Universitetet i Stavanger

AUTHORS: **EDNARD MATHEW CALMA DIZON, NICOLAI GIUSEPPE GRØDELAND**
SUPERVISOR: VIDAR FOLKE HANSEN

Microstructural Analysis and Mechanical Properties of LMD 316L Stainless Steel

Bachelor Thesis in Mechanical Engineering - 2024

Faculty of Science and Technology

Department of Mechanical, Structural Engineering and Materials Science

Abstract

This study aimed to examine the morphology and properties of 316L made in Laser Metal Deposition to address underlying impact of cooling rates and other processing parameters. Furthermore, investigation into its mechanical properties and to compare it with forged 316L. The investigation was conducted using Light Optical Microscopy, Scanning Electron Microscopy, Energy Dispersive Spectroscopy, Electron Backscattered Diffraction, Vickers hardness tests, Charpy v-notch tests and porosity measurements. The LMD process produced almost fully dense metallic part at a relative density of minimum 99.6%. Examination revealed homogenous austenitic microstructure with non-existing ferrite content of .1%. Due to lack of ferrite, cracks were dispersed throughout the material. Its microstructure looked like epitaxial growth of coarse columnar grains and cellular sub grains. This directional solidification from thermal cycle has created an anisotropy in the microstructure. Evident in the tensile values, where x and y-direction have an overall yield strength of 524.2 $\pm$ 7.5 MPa in comparison to z-direction of 418.1 $\pm$ 100.8. However, the controlled grain growth and low heat input produced a grain size ranging between 32-45 μm which aided in having slightly greater mechanical properties and hardness. The Charpy values were consistent, 114.7 ± 2.3 perpendicular to build direction and 113.3 ± 6.4 parallel to build direction.

Acknowledgements

We extend our gratitude to Professor Vidar Folke Hansen, our supervisor, for his guidance and support throughout this thesis. His extensive knowledge and encouragement have been helpful for completing our thesis.

We also express our appreciation to the lab engineers Espen Undheim, Johan Andreas Håland Thorkaas and Mats Ingdal for their guidance on the usage of various lab equipment and sample preparation methodology. In addition, we would like to thank Navid Sayyar for his expertise regarding LMD. Their assistance has been vital in our research.

Special thanks are due to Nordic Additive Manufacturing, especially Sture Henning Sørli, for providing the material that made this study possible. Their support on technical background regarding Laser Metal Deposition has been extensive use to us.

Furthermore, we would like to acknowledge the University of Stavanger for granting us access to various equipment and labs. Finally, we would like to thank our families and friends who have provided us with support throughout this semester.

Nomenclature

AM	Additive manufacturing
BD	Build direction
BCC	Body-centered cubic
CAD	Computer-aided design
CNC	Computer numerical control
DED	Direct energy deposition
DP	Diamond polishing
EBSD	Electron backscattered diffraction
EDS	Energy dispersive spectroscopy
FCC	Face-centered cubic
FG	Fine grinding
LMD	Laser metal deposition
LOM	Light optical microscopy
NAM	Nordic Additive Manufacturing
OP	Oxide polishing
PG	Plane grinding
SDAS	Secondary dendrite arm spacing
SEM	Scanning electron microscope
SE	Secondary electrons
SiC	Silicon carbide

Table of Contents

List of figures

1 Introduction

In recent years, the manufacturing industry has undergone a revolution with the advent of what is termed three-dimensional or (3D) printing, also called additive manufacturing (AM). Unlike traditional subtractive methods such as milling or machining, AM involves the addition of raw material gradually being added, often layer by layer, based on computer-aided design (CAD) data [1]. This innovative approach offers numerous advantages, including enhanced design flexibility, reduced material wastage, and the capability to produce complex shapes and geometries that could not be produced using other manufacturing techniques. In addition to this, AM can reduce the environmental impacts of manufacturing by enabling local production.

Applications of AM are found in just about every field and industry and will undoubtedly continue to escalate dramatically according to [1]. The current utilization of AM spans across a huge range of industries, extending from the automotive industry to aerospace engineering and beyond.

Despite being looked upon as a promising technology, AM has some drawbacks and trade-offs with traditional manufacturing. The mechanical properties of 3D printed parts are often inferior to those manufactured using traditional technologies [1]. It is important that proper research is done into the mechanical properties and microstructure of printed materials.

The alloy studied in this thesis is printed 316L stainless steel manufactured and delivered by Nordic Additive Manufacturing (NAM). The alloy is manufactured using a laser metal deposition (LMD) process which is a subcategory of direct energy deposition. The aim for this thesis was to research the mechanical properties and to analyze the microstructure of the alloy to see whether they align with the theory. All aspects of the research, from sample preparation to other various tests, were done in the laboratories and facilities at University of Stavanger.

We have created all figures and tables presented, drawing inspiration from sources are referenced.

2 Literature study

2.1 Metal Additive Manufacturing

Additive Manufacturing utilizes a layer upon layer material process, commonly known as 3D Printing. It can deposit materials only where they are needed, as opposed to subtractive manufacturing. The principle of subtractive manufacturing is to remove a bulk object to get desired geometry, this change can reduce material waste as well as carbon emissions. Generally, the desired design component is aided with CAD software, which can convert these files into 3D-system files for the machines to scan [2, 19]

In recent times, additive manufacturing has gained popularity. 3D printers that employ plastic or other polymers are prevalent for personal use are as well now being widely integrated into industrial applications. There are several metal-based additive manufacturing methods, but most commonly is to utilize powdered material e.g. Powder Bed Fusion, Directed Energy Deposition, Sheet Lamination, Binder Jetting, and many more [33]. The common factor for these technologies is to create structural parts, that are often in complex geometries, and compete with traditional manufactured parts such as casting or forging. In this study directed energy deposition process is focused.

2.1.1 Laser Metal Deposition (LMD)

The material that was used in this thesis was printed in Laser Metal Deposition. It is a sub-category within Laser-Based DED method, DED being one of the oldest methods, is generally known as cladding [2]. This is a recently developed technique that has its advantages in comparison to traditional printing types. It is known for its versatility for industrial applications that might otherwise require extensive machining, thus resulting in overall costs. Operated in five axes giving flexibility for repairing or adding features with ease [4]. And it employs a blend of process parameters, feed rate, scan speed, laser spot size and power.

It harnesses a high-energy laser beam and metal powder fired through a coaxial nozzle thus resulting in a melt pool onto a substrate; used to melt the deposition to previously deposited layers or damaged structural materials [2]. The deposition process is controlled in an enclosed chamber to minimize interference, a non-reactive inert gas such as Argon, Helium or Nitrogen is blown through the nozzle which not only protects the melt pool but also resists the cladding

deposit from possible oxidation [3]. The focused laser beam provides precise and localized heating with deposition layers ranging from 0.2-1.0 mm thick, allowing for controlled melting [5]. Overall, it is relative to traditional welding.

Since deposited material is ranging approximately 1 mm, it is evident that the heat input is compact being concentrated in a small area. This can facilitate high cooling rate with relatively little heat-affected zone, as the molten metal rapidly solidifies upon contact with the substrate or previously deposited layers. With an undergoing thermal cycle, it is quite apparent that the material is subjected to a possible phase transformation in its microstructure during solidification [3,4].

2.1.2 Powder Material 316L-Si

The powder in this thesis is a product of MetcoClad 316L-Si, designed specifically for laser cladding purposes. It is an austenitic-type stainless steel and low carbon content, which serves to desensitize the clad deposit, thereby preventing precipitation of grain boundary carbide. The chemical composition of the material is given by following table underneath [10].

Table 1: Powder chemical composition used in the material, given in wt%

Fe	Ni	Cr	Mo	Si	Mn	C	Others
Balance	12.0	17.0	2.5	2.3	1.0	0.03	≤0.5

2.1.3 Process parameters and BD

Table 2: Process parameters

Laser Power (W)	Scanning Speed (mm/min) or (mm/s)	Spot size (mm)	Layer thickness (mm)	Powder feedrate (g/min)	Protective Gas
1200	2000 or 33.3	2.0	1.0	25.0	Argon

The 316 was given with each layer oriented perpendicular to the previous layer i.e. 90 degrees as shown in Figure 1. The build direction (BD) progresses vertically in the z-direction. Material inner layers have an outer surface layer acting as a clad which are perpendicular built from the inner layer.

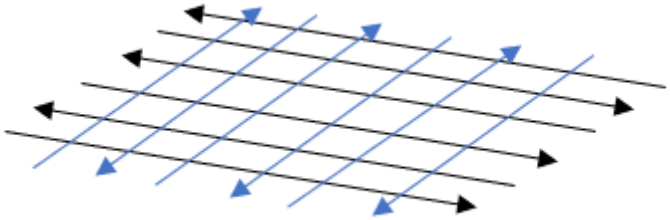

Figure 1: Simplified schematic of how each layer is orientated

2.2 Stainless steel

Pure metals are hardly utilized in their pure form in construction, as they are weak. Often, they are mixed with other elements to improve their overall properties. Stainless steels are known for their good resistance in oxidation especially at normal or elevated temperatures. They can be found everywhere such as kitchen utensils, cutlery, or cookware. It must contain a minimum of 10.5 weight percent chromium and a maximum carbon weight content of 1.2 [7,11]. Generally, categorized into five main types: austenitic, ferritic, martensitic, and duplex [6].

2.2.1 Austenitic Stainless Steel

Austenitic stainless steels are predominant among other stainless steels, as they are frequently utilized in applications needing resistance to atmospheric or slightly elevated temperature corrosion. They have comparable mechanical strength to steel, typically around 210 MPa in minimum yield strength at room temperature. In addition, these alloys showcase favorable low-temperature impact properties especially in cryogenic applications [6].

Austenitic steels are categorized into 2xx and 3xx series Among 3xx series, 304,316, 321, and 347 are the most popular. Their compositions are usually around 18 weight percent chromium and 8-12 weight percent nickel. For L grades, it is denoted as low-carbon types with carbon

content of 0.03 wt%. These alloys showcase enhanced resistance to intergranular attack in corrosive environments [7].

Chromium (Cr): Chromium is applied in steel to fulfill the minimum requirement of 10.5 wt% to be categorized as stainless. It offers good corrosion resistance, promotes ferritic microstructure, and acts as a protective film around the steel that prevents diffusion of oxygen into the surface with unprotected carbon steel. Conventionally, the greater chromium content the greater its corrosion resistance [11,12].

Nickel (Ni): Nickel is essential in 300 series grades as it offers ductility, strength, and toughness at high and cryogenic temperatures. It also reduces the corrosion rate of acid attack in stainless steel, particularly sulfuric acid [11].

Manganese (Mn): Manganese is added to assist de-oxidation, during melting, and to prevent inclusions which can cause hot cracking problems. Manganese is an austenite stabilizer and can replace some of the nickel content in stainless steel [11,12].

Silicon (Si): Silicon enhances resistance to oxidation both elevated temperatures and in highly oxidizing solutions at lower temperatures [11].

Molybdenum (Mo): Addition of molybdenum adds resistance to localized pitting or crevice attack, particularly in Cr-Fe ferritic grades. It aids in resisting oxidation of chlorides. Often, the higher contents offer better resistance to higher chloride levels [11,12].

Carbon (C): Carbon improves overall mechanical strength and hardness. However, carbon content needs to be regulated since undesirable amount led to the formation of chromium carbides at grain boundaries. [7].

2.3 Diagrams

2.3.1 Iron-Carbon Phase Diagram

According to [29] all studies of the constitution and structure of all steels and iron must first start with the iron-carbon equilibrium diagram. The basic feature of the diagram influences the behavior of even the most complex alloy steels. It provides valuable insights into the phase transformations that occur as a function of temperature and carbon content. This knowledge is essential for optimizing processing parameters and controlling the microstructure and mechanical properties of iron-carbon alloys.

Figure 2 shows a portion of the iron-carbon phase diagram relevant where the red vertical line represents the carbon content of 316L.

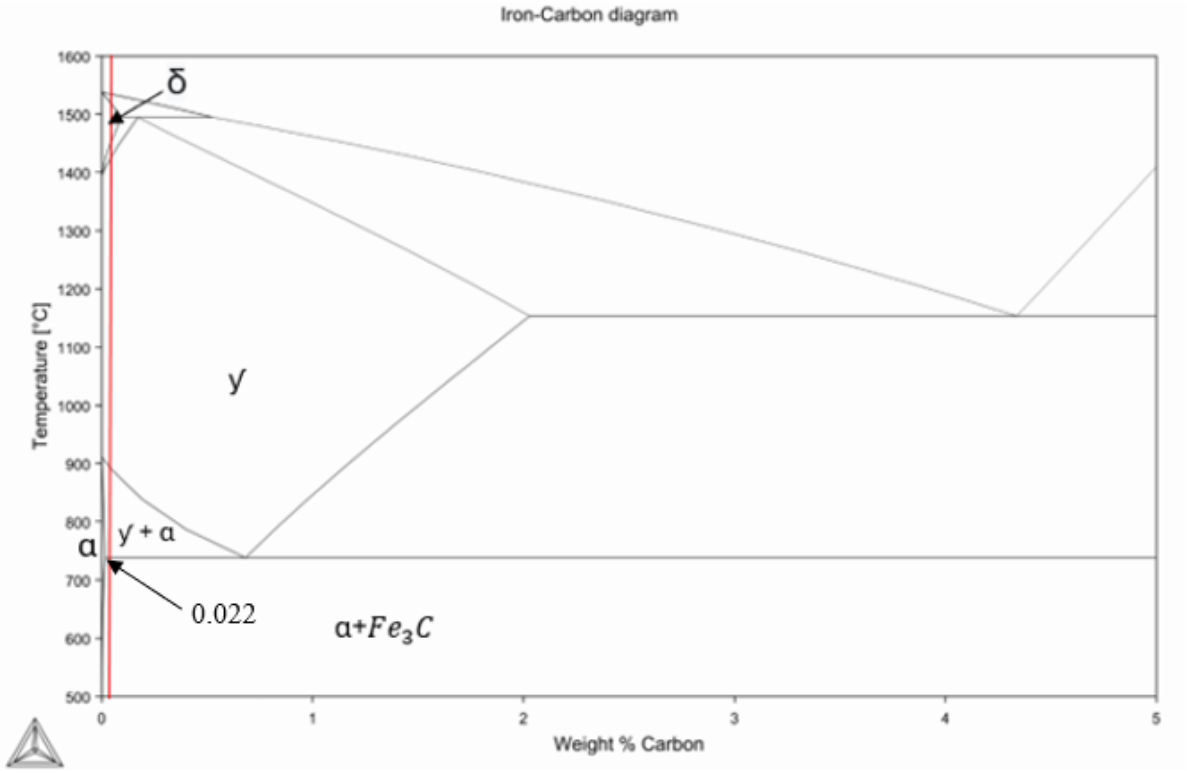

Figure 2: The iron-carbon equilibrium diagram. Diagram made in Thermo-Calc.

2.3.2 Schaeffler Diagram

The constitution diagram, or simply known as Schaeffler Diagram is a tool used in metallurgy to predict the microstructure of welds in stainless steels. It considers the chemical compositions of the material to estimate the phases that will form during welding and casting after cooling from a high temperature. The diagram divides the composition into regions representing austenite, ferrite, martensite, or a combination of phases. In this case, it is used to predict levels of ferrite present in the austenitic stainless steel depending on the alloying element that was used. The diagram makes it possible to make an estimation of total ferrite and austenite based on determining the chromium-nickel equivalents, given in equations 1 and 2.

Equation 1

$$Cr_{eq} = \%Cr + \%Mo + 1.5\%Si + 0.5\%Nb + 2\%Ti$$

Equation 2

$$Ni_{eq} = \%Ni + 30\%C + 0.5\%Mn$$

Plotting the weight percent of the powder material in their respective alloying elements in the equations will give an intersection. As the point indicates, the microstructure may contain ~10% ferrite [7, 21].

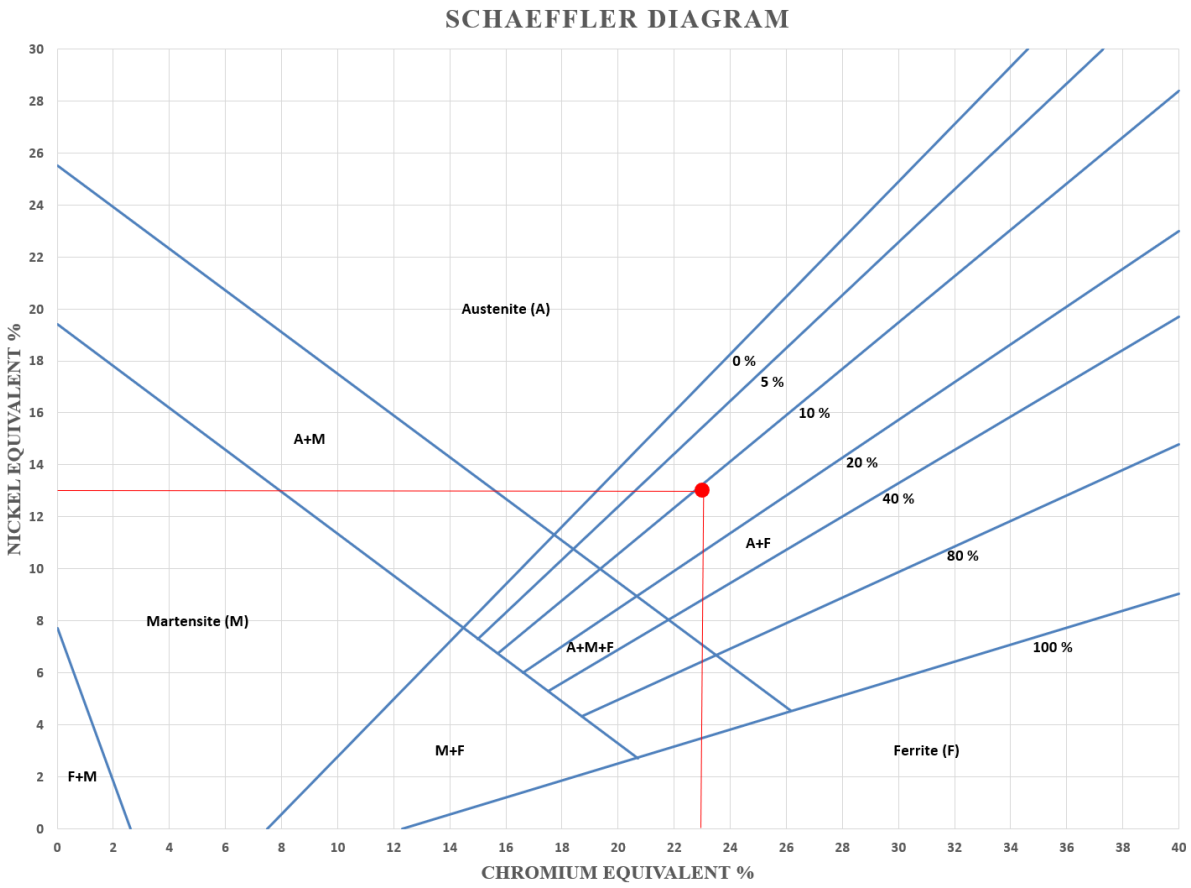

Figure 3: The constitution diagram, nickel and chromium equivalent plotted in red [7]

2.4 Microstructural Morphology and Solidification Dynamics

Austenite (γ-iron): Austenite is the primary phase and can be identified by its Face-Centered Cubic (FCC) structure. It quickly develops at high temperatures usually above the eutectoid temperature of 723°C [1].

Ferrite (α-iron): Ferrite is the secondary phase and can be identified as a Body-Centered Cubic (BCC) structure for the 316L. It improves strength, especially at lower or cryogenic conditions [1].

δ-Ferrite: Is a high-temperature version of ferrite formed during solidification. They develop at higher temperatures where they either transform to austenite or remain within the grain boundary, depending on cooling rates. It prevents hot cracking [6, 29].

Carbides: Carbides, particularly $M_{23}C_6$, form in grain boundaries during cooling. It has its advantages and disadvantages; on the good side they offer corrosion resistance. However, once the material is at an elevated temperature at which supersaturated austenite state occurs, micro segregation happens which cause diffusion in the material. These carbides will deplete chromium content in the layer matrix and will become fragile to corrosion once it bypasses below the minimum content [6, 29].

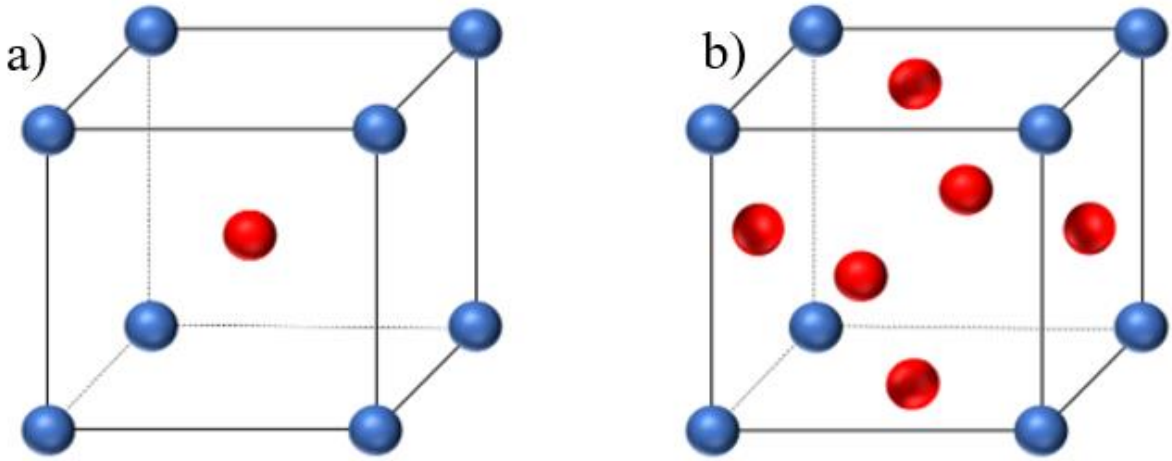

Figure 4: a) Body-centered Cubic Unit Cell (BCC) and b) Face-centered Cubic unit cell (FCC)

2.4.1 Solidification Dynamics

In general, the structure of metal casting comprises of three distinct regions, Figure 5 [20, p.233-234]. As the melt pool transitions to liquid-solid phase, a process called nucleation initiates, where atoms are gathered at specific areas causing unit cells to form. This transformation is called crystallization, that is a formation of many small crystals into polycrystalline. As the molten pool further cools down and solidifies, they set a random crystallographic direction and expand; eventually interfacing with other crystals [1].

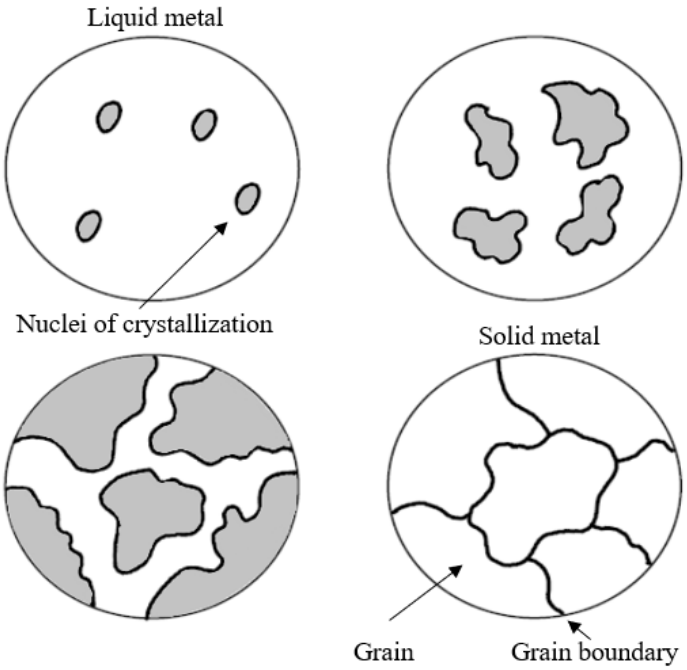

Figure 5: Microstructural changes during solidification of a metal [40,41].

(1) Chill Zone: This initial solidification zone. It involves small and randomly oriented crystals dispersed near the mold wall with various orientations.

(2) Columnar Zone: These are elongated crystals that grow parallel to the direction of heat flow. This is essential for evaluating directional solidification and its influences on mechanical properties.

(3) Equiaxed Zone: Random crystallization of grains for the remaining molten metal. It generally provides insight into nucleation and growth once solidified [20].

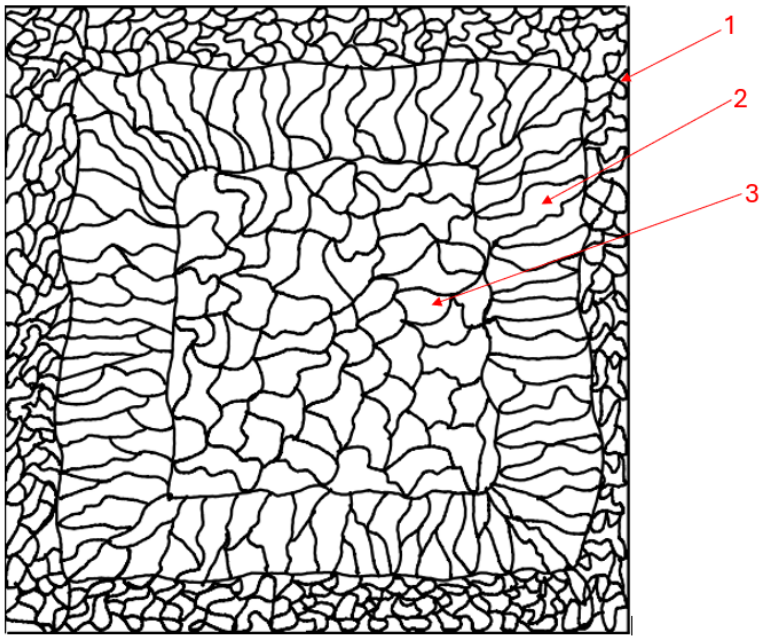

Figure 6: (1) Chill zone, (2) Columnar zone and (3) Equiaxed zone [42]

Each crystal structure formed is called a grain and their interfaces or where they collide are called grain boundaries. However, there can be development of smaller cells within each grain, called sub-grain. The microstructure is greatly influenced by the effects of alloying elements and processing methods e.g. casting or welding. Cooling rate dictates the final microstructure morphology [8].

Dendrites appear like a tree-like structure often long and thin; they form during liquid-solid transformation. It has secondary and sometimes tertiary arms that grow along favorable crystallographic orientation because of localized differences in the temperature. For cubic metals, it has preferential growth comparable to columnar grains [26].

High cooling rates favor more of a cellular arrangement, displaying a honeycomb mesh [8]. Secondary Dendrite Arm Spacing (SDAS) is crucial for determining the cooling rate; as faster ones lead to a finer SDAS, while slower cooling results in coarser SDAS. Finer SDAS has been found to increase strength and hardness, since it leads to a more refined grain structure.

Secondary Dendrite arms can be quantitatively measured using the following equation from [9]:

Equation 3

$$SDAS = \frac{L}{N-1}$$

Where L is the distance from the first observed dendrite arm to the last, N is the amount of dendrite arms.

Cooling rate regarding to secondary dendritic arms:

Equation 4

$$\lambda_2 = 25(\varepsilon)^{-0.28}$$

This was empirically tested and conducted on 300-grade stainless steel under same condition [8, 27]. Whereas λ_2 is represented as SDAS and ε for cooling rate. In addition, micro segregation occur during elevated temperature causes element diffusivity. For instance, type 304 and 316 solidifies as homogenous Austenite; Cr and Mo tend to partition in sub grains boundaries [8].

2.4.2 Types of Solidification

In layer-by-layer additive manufacturing, epitaxial solidification occurs. This is when a new layer of liquid metal solidifies along with the substrate. Long columnar grains perpendicular to the temperature gradient develop because of this process, resulting in existing grains from the previous substrate expanding. This process is caused by thermal cycle that occurs during deposition, in which the molten metal's high temperature partly remelts the substrate, allowing the grain to elongate beyond the fusion boundary [28].

Solidification of 316L stainless steel can occur in several modes based on composition and cooling rate: Single-Phase Austenite (A), Primary Austenite with Second-Phase Ferrite (AF), Eutectic Ferrite and Eutectic austenite (E), Primary Ferrite with Second-Phase Austenite (FA) and Single-Phase Ferrite (F). These types can be identified through microscopy after metallurgical preparation [8, 27].

2.4.3 Texture and Anisotropy

As mentioned previously, metals consist of grains and boundaries in their solid state. Within a polycrystalline, each grain represents an individual crystal with distinct lattice orientation. The general principle to understand metal additive manufacturing is to understand the fundamental of solidification process in casting. Simply, casting and LMD both share similar characteristics as it involves melting. During solidification in castings, columnar grains develop along specific crystallographic directions, shown in Figure 6, resulting in a preferred orientation or so-called texture. The application of heat or mechanical treatment can change the texture of these materials [20]. Therefore, a material with texture typically demonstrates anisotropic properties. On the other hand, independent grains with scattered orientation are called isotropic [1, p.73]. In the case of FCC metals and alloys, such as 316L, a <100> direction is preferred with columnar grains or perpendicular to the mold wall. Pole figure analysis is a possible method in scanning electron microscopy to investigate orientation of grains [14].

2.4.4 Defects in LMD-Build Materials

There are several defects that can occur in additive manufactured materials. Defects such as bonding, presence of pores or even oxide entrapment are common [3]. In the case of bonding defects, inadequate fusion or melting between adjacent layers. Improper melting can be processing parameter defect such as poor scanning speed or laser power. Formation of these defects can lead to crack initiation during strain, thus reducing its overall mechanical properties.

2.4.5 Grain Size Strengthening

Properties of material can be controlled by controlling its grain size. By reducing the grain size, this led to an increased number of grains in the system, thus increasing the number of boundaries. It increases overall properties and hardenability because dislocation is impeded due to shorter distances of these boundaries. This relationship is described by the Hall-Petch relationship, which states that yield strength increases inversely with the square root of the grain diameter. This phenomenon is because smaller grains provide more grain boundaries, which impede dislocation movement, thus enhancing mechanical properties [1, p.212-213]. This relation can be described by this formula:

Equation 5

$$\sigma_y = \sigma_0 + k_y d^{-\frac{1}{2}}$$

Where σ_0 is the lattice friction stress to move dislocation, k_y is constant and d is the average grain diameter of the material.

2.5 Mechanical Tests Equipment

2.5.1 Tensile Testing

Tensile testing is important in determining several mechanical properties of materials that are crucial in design. During this test, a specimen undergoes deformation, usually until fracture under a steadily increasing tensile load applied uniaxially along the long axis of a specimen. The specimen in a tensile test is usually circular, with the diameter reduced in the middle portion. This configuration is chosen so that the deformation is confined to the narrow center

region. A tensile testing machine elongates the specimen at a constant rate, while measuring the applied load with a load cell, and the elongation with an extensometer. The relationship between the applied load and the resulting deformation is typically presented graphically as a stress-strain curve. The results yield information about the materials' yield strength, ultimate tensile strength, modulus of elasticity and ductility [39].

Offset Yield Strength point (Rp 0.2%):

This is the required stress for dislocation or plastic deformation to happen. Often, it is difficult to determine a clear yield point that marks the boundary between elastic- and plastic deformation, as it smoothly transitions between the regions. Thus, the Offset Yield Strength can be determined to roughly estimate the transition from elastic to plastic strain. By creating a line parallel with a more linear section within the elastic region, towards the right of strain axis at [$e = 0.002 mm/mm = 0.2\%$], the point where they intersect should determine its "offset yield-point" [14, p.190].

Ultimate Tensile Strength (Rm) and Elongation:

The highest recorded engineering stress is on the stress-strain curve as it exists in the plastic deformation region, where material undergoes permanent elongation. This stress level marks the point at which necking occurs in the test piece. In plastic region, various materials behave distinctly showcasing whether they have ductile or brittle behavior.

2.5.2 Impact Testing

In a Charpy test, a standardized specimen in the form of a rectangular bar with a V-notch machined into it is subjected to a sudden impact from a swinging pendulum. The notch serves as a point of stress concentration. The specimen is securely clamped at its base, and the pendulum armed with a hammer is released from a specific height to strike the specimen. The energy absorption, calculated from the difference between the potential energy at the initial height and end point is a measurement of the impact energy. The Charpy test results typically report if the material is brittle or ductile. Further examination of the fracture can be seen on both a macroscopic and microscopic level to provide additional insights into the material's behavior under impact loading [39].

2.5.3 Vickers Hardness Test

The Vickers hardness test assesses a material's resistance to plastic deformation by pressing a pyramid-shaped diamond into its surface. The pyramid's sides form an angle of 136°, from which the lengths of the diagonals are measured as shown in Figure 7 a) and Figure 7 b). These measurements, along with the applied force, allow for the calculation of hardness in HV units.

Equation 6

$$HV = 1.854\ \frac{P}{d^2}$$

Where P is the force, and d is the length shown in Figure 7 b).

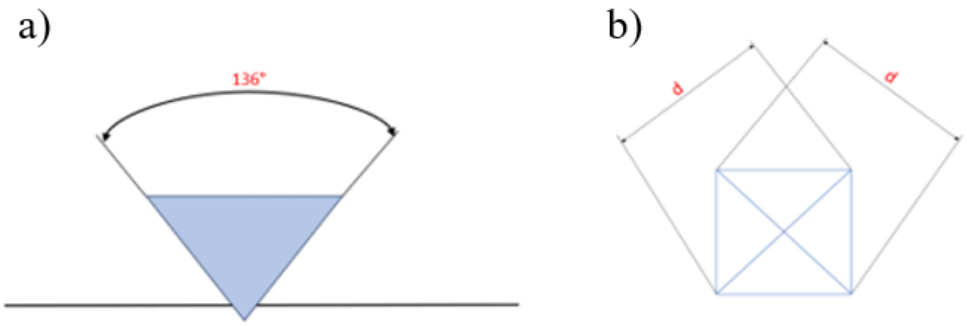

Figure 7: a) Side view indentation and b) top view indentation [p.175,1]

2.5.4 Density Analysis

Density analysis is important to examine the number of pores within the material. For instance, Archimedes principle served as a quintessential tool, which involves the general principle of buoyant force of an object when it is immersed in a fluid. Simply, the test piece was weighed in its current state and in water using this equation found in [18].

Equation 7

$$\rho = \left[\frac{M_o}{M_o - M_w}(\rho_w - \rho_o)\right] + \rho_o$$

Denoted by M_o and M_w are the weight of the test piece in air and water at room temperature, respectively. And the densities of water and air are denoted by ρ_w and ρ_o, that are 1 $\frac{g}{cm^3}$ and 0.001225 $\frac{g}{cm^3}$ respectively [17]. The relative density was calculated to a standardized density of 316L, which is 8.00 $\frac{g}{cm^3}$ [15,16].

Equation 8

$$RD\ \% = \frac{\rho_{meassured}}{\rho_{standard}} * 100$$

However, gas pycnometer is another tool used during experiments. In general, it measures material's bulk volume via gas displacement to determine its overall density. This tool is quite practical and offers higher accuracy and precision, since it can even reach the smallest pores within the material, especially in stainless steel. In Figure 8, the procedure of machine is illustrated. There are three valves involved in this process: (V1), (V2) and (V3). In V1, it sends gas, such as Helium, into the sample chamber; V2 transports this gas and expands the reference chamber, and lastly V3 expels the gas into the atmosphere [22].

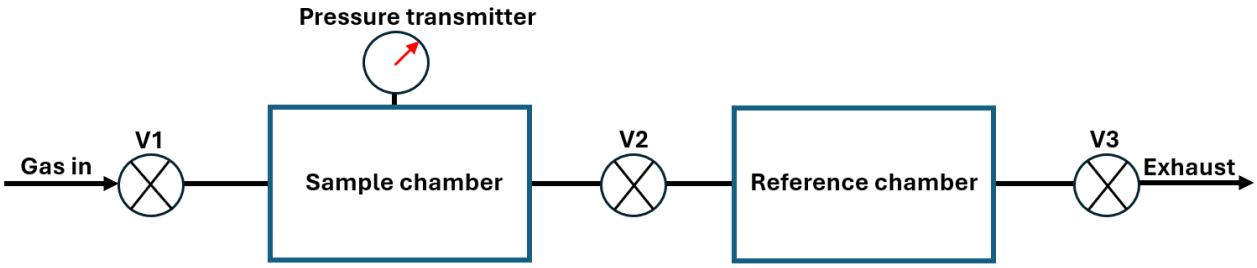

Figure 8: Schematic of flow diagram of a gas pycnometer design [22]

2.6 Microstructure Analysis Equipment

Microscopic examination was used to illuminate the microstructural features, including constituent grains and defects of the specimen. The equipment utilized in this study is optical- and scanning electron microscope.

2.6.1 Light Optical Microscope

Light Optical Microscopy or LOM, magnifies, and reflects basic elements of the metal under visible light. It is suitable to study surface properties, rough structures, and shape at macro- and microscopic level by the difference of reflectivity at various regions in the structure. A thorough preparation onto the surface is crucial to achieve the most effectiveness of reflection. The surface of interest must undergo metallographic ground and polishing procedures with the usage of finer abrasive papers. The effectiveness of the preparation can be addressed by achieving a mirror-like surface finish [1]. In addition, an electrolytic process called etching is used as it enhances the contrast on surfaces, revealing greater microstructural details that would not be seen evidently on as-polished level. The objective is to corrode the material at different rates depending on the grain orientation and chemical composition. Due to variations of corrosion attack, alteration in angle and depth of the surface occur, thus resulting a contrast of dark and light regions when reflected under visible light.

2.6.2 Electron Microscope

An electron microscope exerts a beam of accelerated electrons in a vacuum for illumination. As electrons gain high velocities, they showcase wave-like behavior, with a wavelength proportional to the velocities. This special type of instrument capable of higher magnification is difficult to observe under OM since it is limited to magnification of roughly 2000 times. This higher magnification in the area, up to 0.003 nanometers, provides higher resolution of images [1, p.109].

2.6.3 Scanning Electron Microscope (SEM)

A concentrated electron beam is utilized by a scanning electron microscope (SEM) to look at the surface of a test piece. When electrons from the machine collide with sample’s atoms; reflected beam (EBSD) is collected and to produce an image. In addition, the composition of the material can be studied with an integrated dispersive spectroscopy (EDS). SEM is used to

reveal grain sizes not seen evident in LOM or grain orientations. Because of its high resolution, SEM is an advantage when examining microstructures such as 316L. The surface under study should be polished, but for the electron beam to interact with it, it must be electrically conductive. Magnifications can range from 10 to an excess of 50,000 times are possible, this high resolution of SEM is valuable for microstructural analysis of surface, with usage of secondary electrons (SE) [1, p.111].

2.6.3.1 Electron Backscatter Diffraction (EBSD)

In EBSD, a fluorescent screen is used to detect the pattern formed by the diffracted electrons, which are blasted through a crystalline sample that is tilted usually at a 70° angle. Crystal structure and orientation at the interface between the electron beam and the sample define the diffraction pattern. Thus, the crystal orientation may be determined from diffraction pattern. In general, EBSD can give an overview of these grains and their respective orientations, identify phases as well as reveal textures [23].

2.6.3.2 Energy Dispersive Spectroscopy (EDS)

Energy Dispersive Spectroscopy is software often integrated in SEM. In essence, it generates information about the chemical composition of a test piece. When an electron beam strikes the inner shell of a distinct atom, it leaves behind a positive charged one. Electron from the outer shell is drawn to this displaced electron to fill the void. The energy that electron releases is unique to the atomic structure of the element. As a result, data that was generated is converted into the software of SEM [24].

2.6.3.3 Secondary Electron (SE)

Secondary electrons produce topographic information of the test piece’s surface in nanoscale. Less energy is needed here in comparison to backscattered electrons because of the inelastic interactions between the main electron beam and the material [25].

3 Experimental procedures

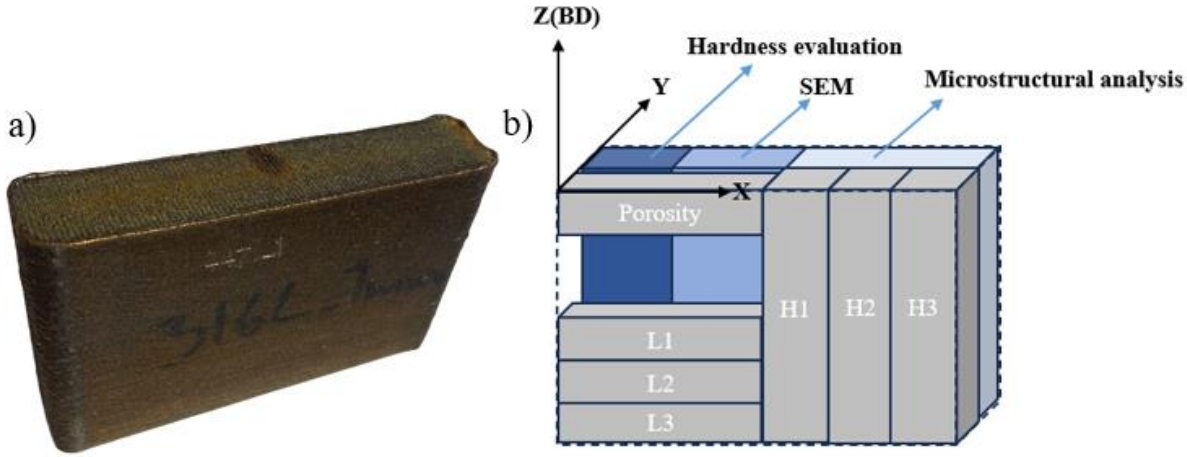

Figure 9: a) Material as received by NAM and b) early-stage sketch prior to cutting

The dimensions of the material received as seen in Figure 9 a) are approximately 96x20x56mm. To perform analysis on the material a sketch was drawn on how to cut the material to best utilize the piece. There were a few alternatives, but it ended up being cut as seen in the sketch in Figure 9 b). All the main cuts were done in a Struers Discotom-10, a machine with great cooling capabilities to prevent heat that could affect the microstructure of the material.

Before the use of the labs and facilities at University of Stavanger, a safety job analysis was written and approved by the lab engineers.

3.1 Charpy preparation and execution

Two sets of three specimens, in different orientations were prepared for Charpy V-notch impact testing, named L1-3 and H1-3 as seen on Figure 9 b). The tests were carried out and dimensioned according to NS-EN ISO 148-1:2016 [37] and the tests were done at -18ºC according to ASTM A182/A182M-23 [38].

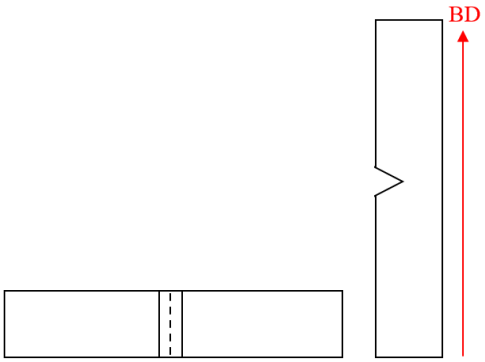

Figure 10: Charpy and V-notch orientation.

The specimens were cut out using the Struers Discotom-10 as seen in Figure 11 a) using an alumina 30A25 cutting wheel as recommended by Struers based on the hardness of the material [35, p.45]. The cuts were made at the lowest possible feed speed of 0,05mm/s.

To get the desired tolerances seen in Table 3, the cuts in the Struers were over dimensioned and the specimens were milled to the correct dimensions as seen in Figure 11 b). The milling machine was configured as recommended by [34, p.51]. Lastly, the V-notch was cut with a CNC machine. All the tolerances were met and were measured with a micrometer.

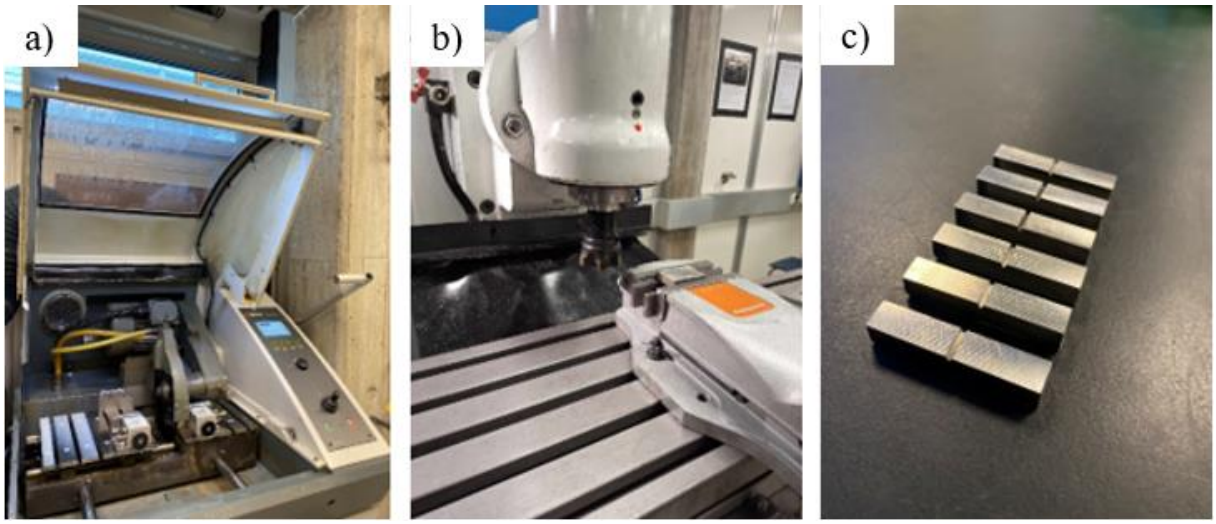

Figure 11: a) Struers Discotom-10, b) milling of charpy specimens and c) charpy specimens

Table 3: Charpy dimensions and tolerances

Designation	Nominal Dimension	Machining tolerance
Length	55 mm	± 0,60 mm
Height	10 mm	± 0,075 mm
Width	10 mm	± 0,11 mm
Angle of notch	45°	± 2°

The Charpy specimens were cooled in a mixture of glycol and ethanol in the Julabo FR89, shown in Figure 12 a) before the specimens got impact tested on a Zwick/Roell RKP450 as shown in Figure 12 b). A self-centering Charpy tong was used to transfer the specimen from a cooling bath to the impact machine. There was an average of four seconds between the specimen leaving the bath, and the hammer hitting the specimen. The absorbed energy was measured by a combination of electronic and analog displays, where the air and bearing friction is accounted for.

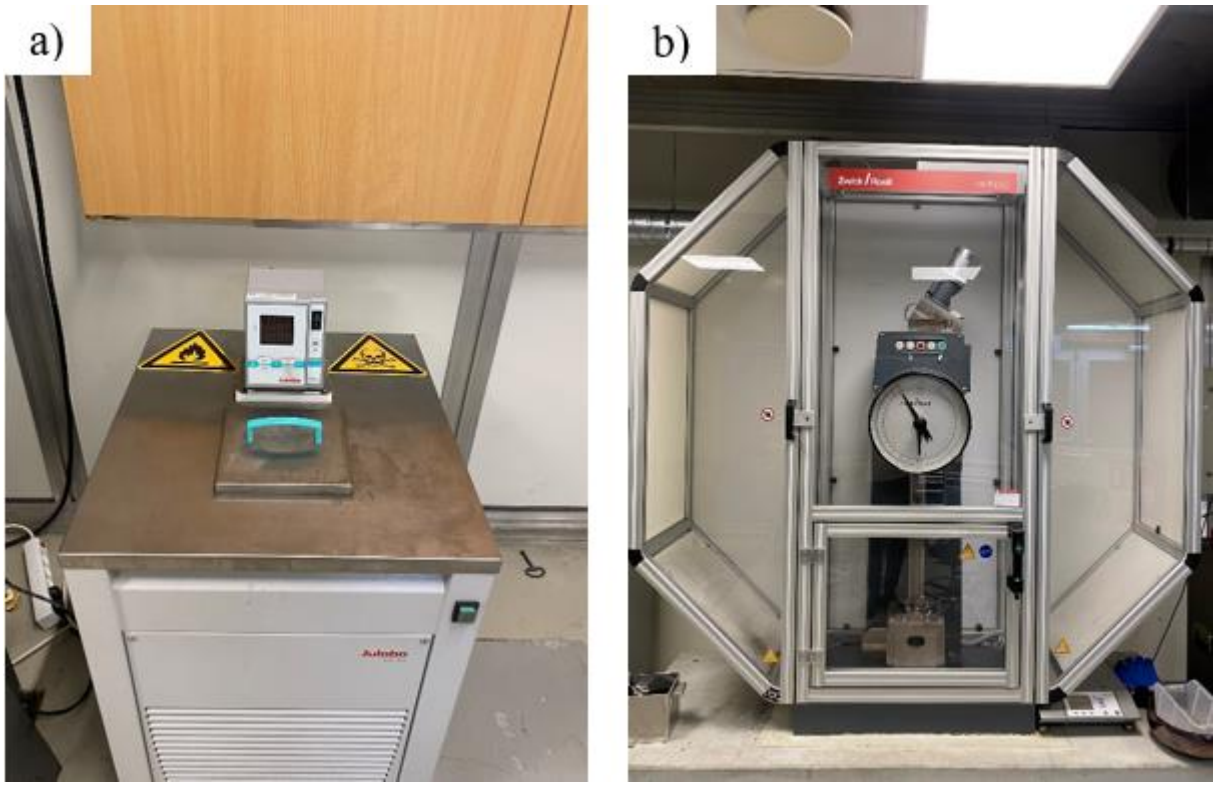

Figure 12: a) Julabo FR89, and b) Zwick/Roell RKP450

3.2 Hardness evaluation

Hardness evaluation was performed on a InnovaTest Falcon 5000, applying a 10 kg HV force with a 10-second dwell time for the indentation.

Prior to test the specimen was mounted in epoxy, and the surface was grounded as according to NS-EN ISO 6507-1:2023 [43]. There were at least 3 diagonal widths between indentations. The hardness evaluation must be carried out on an even and smooth surface, free from foreign material and lubricants. The machine was programmed to perform 44 indentations. The machine automatically calculated the hardness values and took pictures of the indentations.

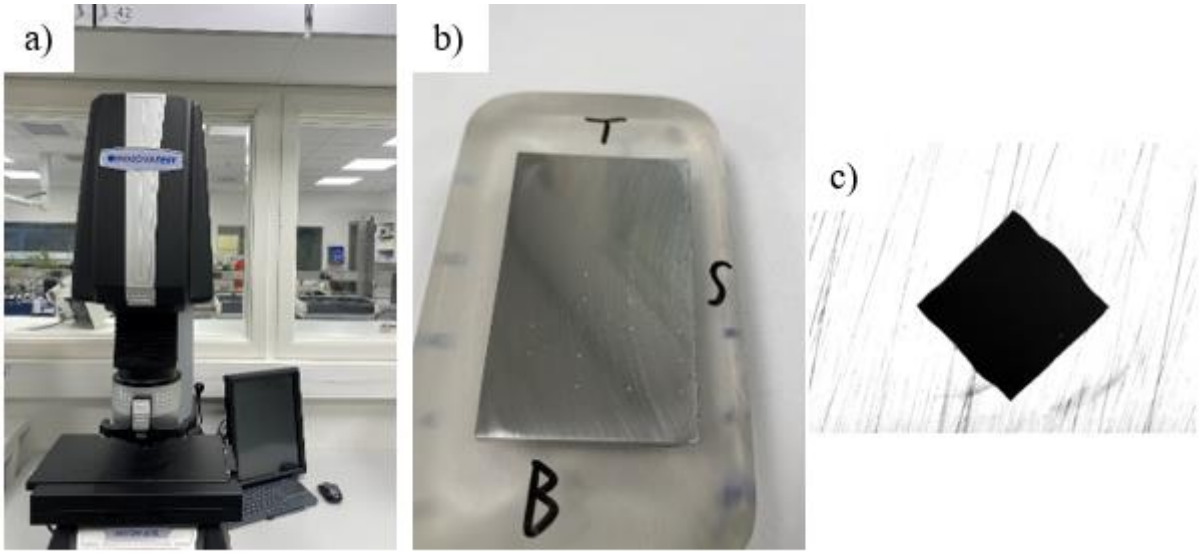

Figure 13: a) InnovaTest Falcon 5000, b) Surface with indentations, and c) example indentation

3.3 LOM preparation and examination

After cutting, a copper piece was welded onto the specimen to allow for electrolytic etching. Then, it was mounted in epoxy for easier handling during grinding and polishing.

The specimen was grinded and polished manually on the Knuth-Rotor 2, initially using method D from [35, page 23]. The outcome of this process was inadequate and led to adding a few additional steps along with grinding and polishing for longer to achieve a good result. A summary of the final procedure can be found in Table 4. The specimen was cleaned in between each step using hot water, followed by ethanol and lastly blow-dried.

Table 4: Summary of final procedure

Steps	Surface	Specification	Lubricant	Time
1	SiC-paper 220	PG	Water	Until plane
2	SiC-paper 320	PG	Water	10
3	SiC-paper 500	FG	Water	12
4	SiC-paper 1000	FG	Water	12
5	MD-Allegro, 9 μm	FG	Lubricant Blue	10
6	MD-Dac, 3 μm	DP	DR-Suspension	10
7	MD-Chem	OP	OP-S	8

To enhance the visibility of material surface details, the specimen was etched with 10% aqueous oxalic acid for 25 seconds at 15V. This method was influenced by [36, p.37], and yielded great microscopic results. As seen on Figure 14 b), the specimen was etched differently at various locations due to its size exceeding the capacity of the machine. However, the microscope revealed good results.

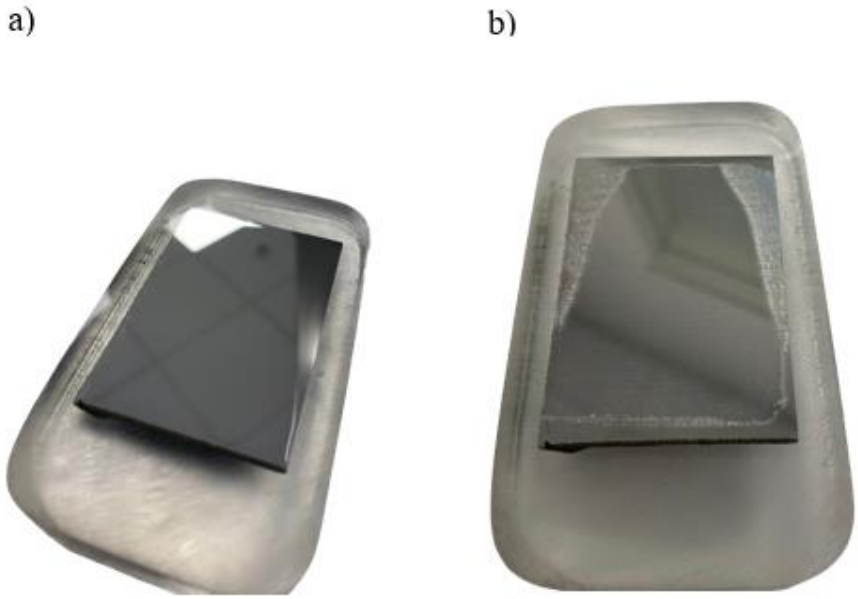

Figure 14: a) Surface pre etching and b) surface after etching

The micrographs at various locations and magnification are taken and processed on an Olympus GX53 with integrated imaging software PRECiV from Evident.

3.4 SEM preparation and examination

Six specimens were extracted for examination in SEM, taken throughout the height of the material as illustrated in Figure 15, along with their orientations.

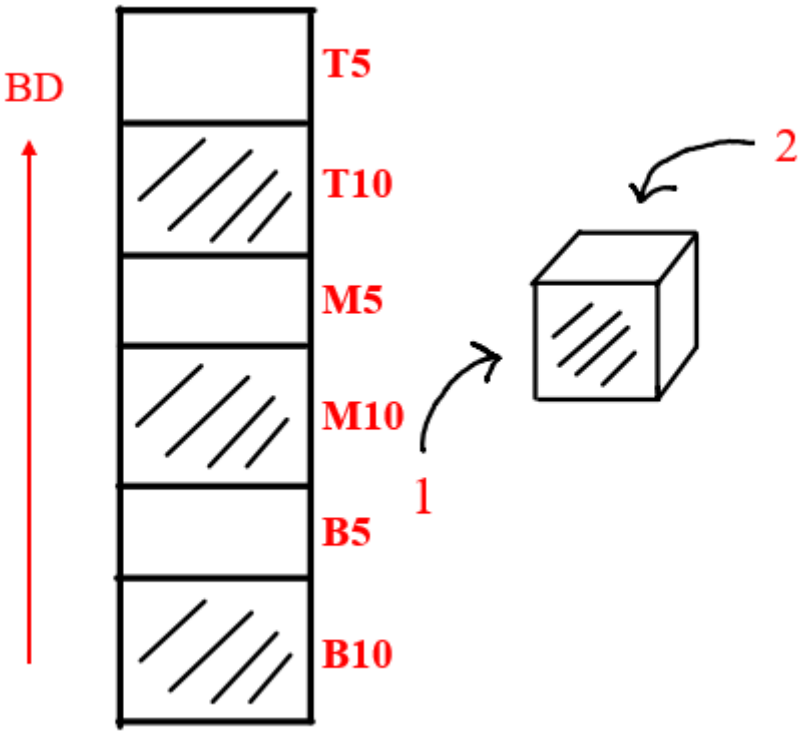

Figure 15: Sketch of SEM specimens

After cutting, the specimens were thoroughly cleaned before being cast in a cylindrical shape using a Struers Citopress-30 machine with Polyfast to allow for conductivity. The shape allowed for the use of the automatic grinding and polishing machine Struers Tegrapol-35, with the use of an automatic lubricant system called Tegradoser-5. The grinding and polishing process was suggested by a fellow student, and a summary of the process can be found in Table 5. The specimens were ultrasonically cleaned between each step in Struers Lavamin.

Table 5: Summary of final procedure

Steps	Surface	Specification	Lubricant	Time (min)
1	SiC-paper 120	PG	Water	2
2	SiC-paper 220	PG	Water	2
3	SiC-paper 320	FG	Water	3
4	SiC-paper 500	FG	Water	3
5	SiC-paper 1000	FG	Water	4
6	SiC-paper 2000	FG	Water	4
7	SiC-paper 2400	FG	Water	4
8	MD-Mol	DP	3 μm diamonds	5
9	MD-Nap	DP	1 μm diamonds	10
10	MD-Chem	OP	OP-S	7

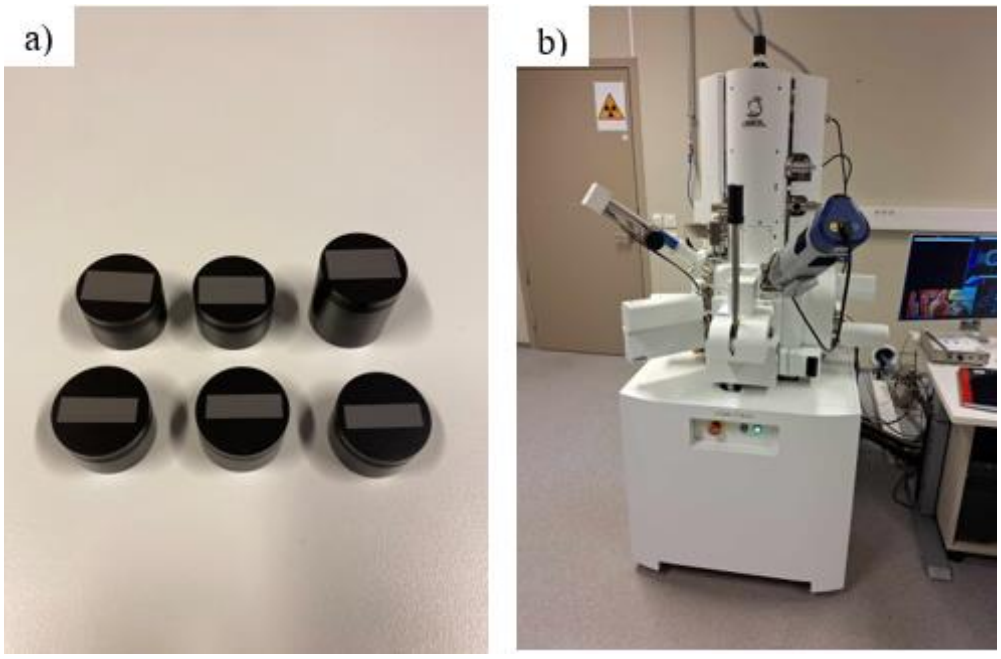

Figure 16: a) Specimens after preparation, and b) JSM-IT800

Lastly, data was collected from SEM using JSM-IT800 including embedded EDS and EBSD software from JEOL.

3.5 Density

A porosity specimen depicted in Figure 9 b) weighing 65.5g was analyzed using the gas pycnometer Accupyc II 1340. The machines manual was followed to conduct the analysis. Additionally, small sections were extracted from L1 and L3 Charpy samples post-fracture to assess the material's overall porosity using Archimedes method. In essence, the test pieces were weighed in their current state and in water using equation as discussed in the literature review.

5 Results

5.1 Microstructural Study

In Figure 17, This image shows epitaxial grain growth that extends beyond the fusion line, with notable coarse columnar grains and cellular grains that are consistent along the fusion boundary. The columnar grains appear significantly elongated, a result of the thermal cycle experienced which involved cooling and reheating from the molted pool as substrate act as a heat sink. In Figure 18 the microstructure showcases homogenous austenitic, as revealed by successful etching, showing sub-grains at a higher magnification within the fusion boundary. This observation is consistent with reported literature findings [8,27]. In Figure 19, the secondary dendritic arms aligned perpendicular to the fusion line, indicating directional solidification.

Additionally, track widths and cooling rates were quantitatively measured using ImageJ; an average track width of 830 μm at the top region 760 μm at the bottom region was discovered from the test piece for LOM shown in Figure 9b)-14. This variation may likely be of heat accumulation from the substrate that acts as a heat sink; Figure 20 shows an overview of these fusion lines. Furthermore, applying the cooling rate formula and SDAS (Method D) [9]. A cooling rate estimate of 8200 K/s in the bottom area and 6800 K/s in the top area was obtained.

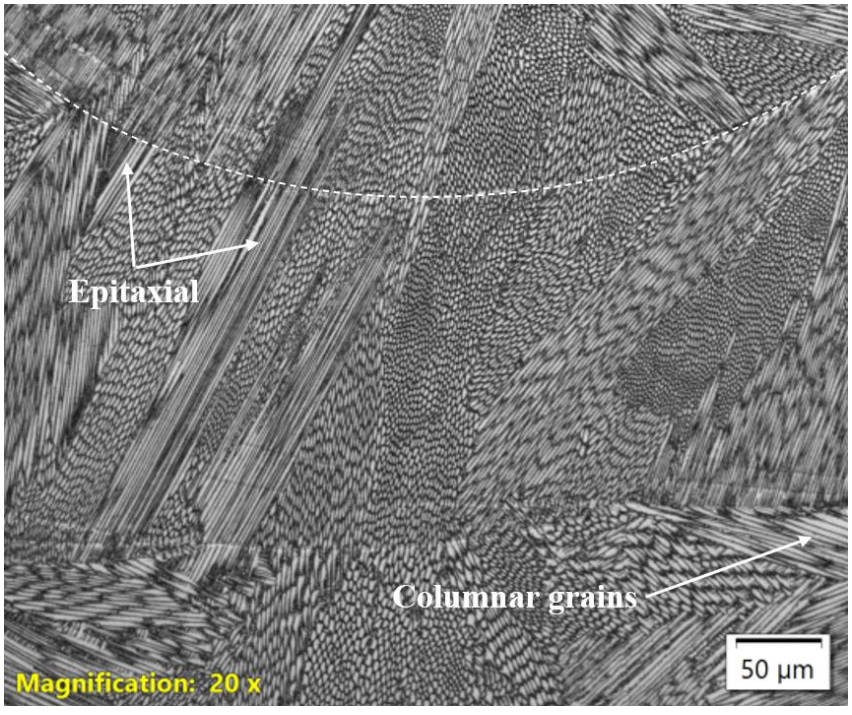

Figure 17: Epitaxial and columnar grains, white dotted line is the fusion line

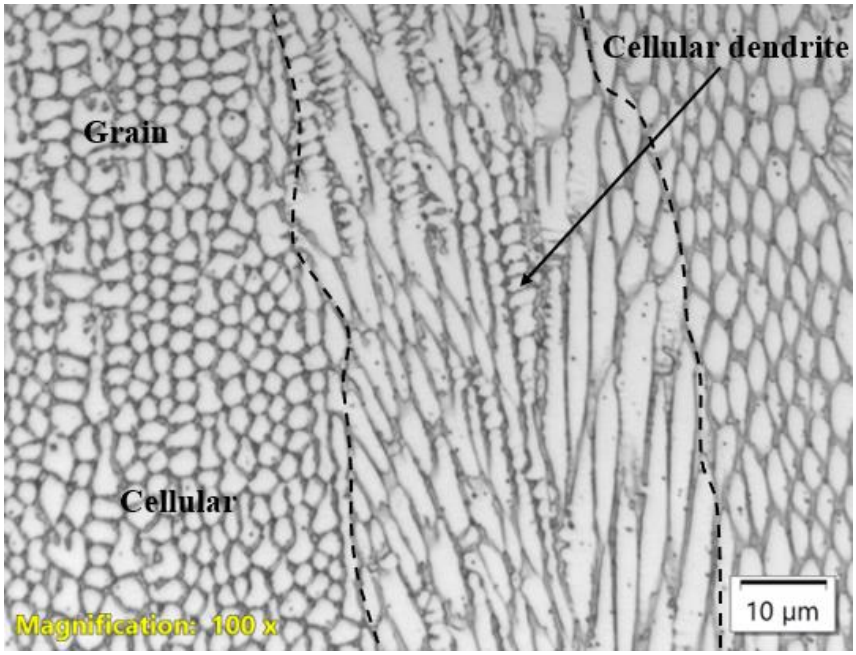

Figure 18: Cellular dendrites, cellular grains and the black dotes lines are grain boundary

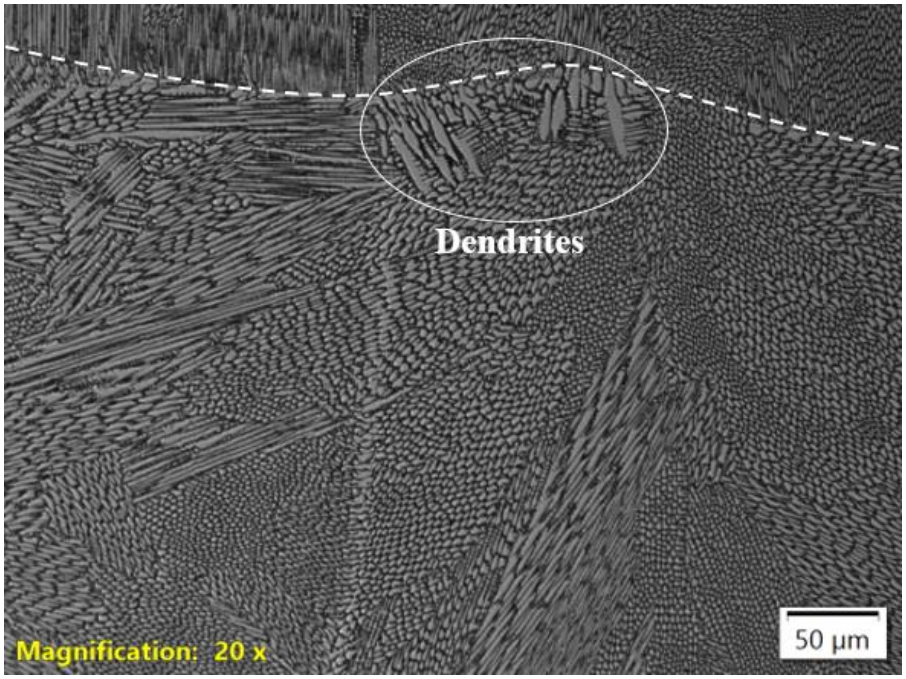

Figure 19: Secondary Dendrite Arms

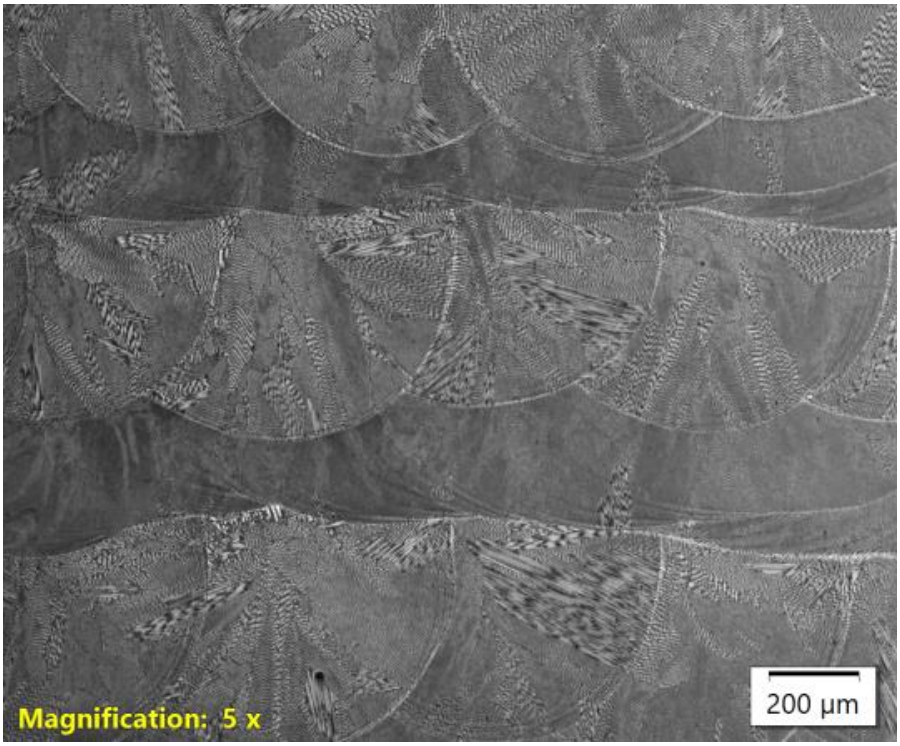

Figure 20: Overview of fusion boundaries

5.2 Scanning Electron Microscopy Results

The average confidence index of the results in all SEM procedures was 0.81. In Figure 22 for test piece B10, a local heat affected zone is prominent. Within the highlighted rectangular box, the columnar structures appear elongated and are observed bypassing the fusion lines. These findings are consistent with those depicted in Figure 17. Figure 23 is a pole figure, demonstrating a strong preferential orientation exhibiting a texture within the <001> direction along the build direction. This texture is an indication of the material's potential anisotropic behavior.

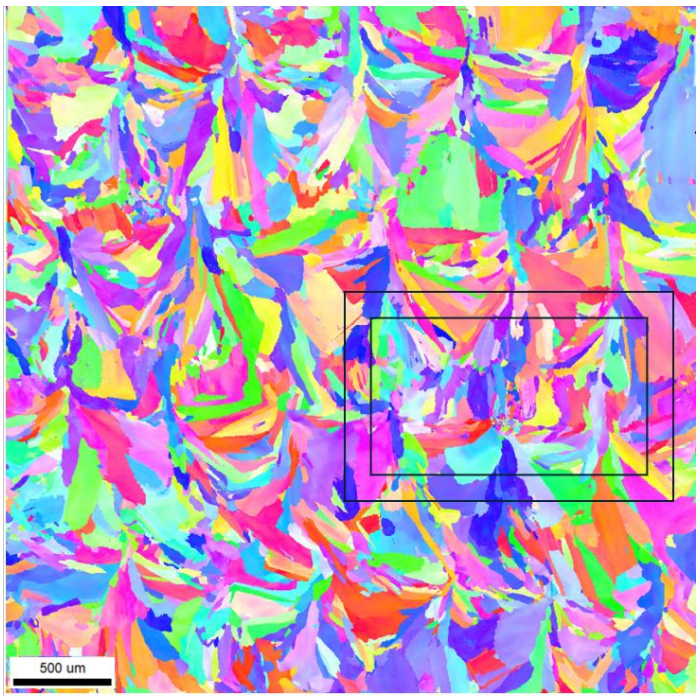

Figure 21: EBSD mapping of grain orientation.

Figure 22: From sample B10, visible columnar grains overlapping the fusion boundary due to epitaxial solidification.

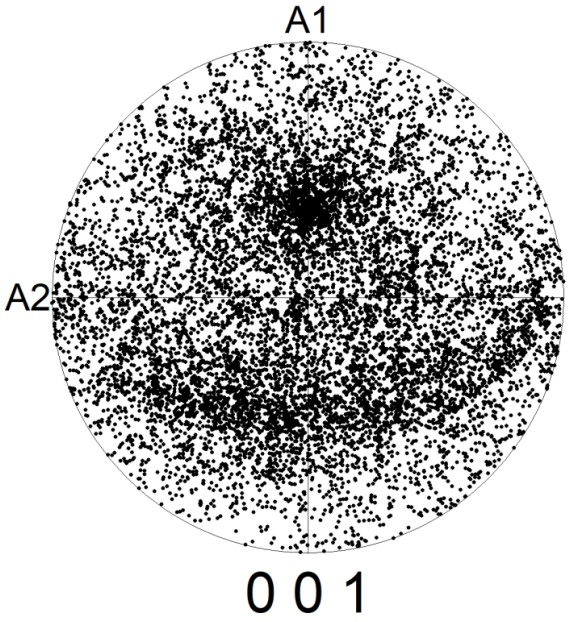

Figure 23: Pole Figure for sample B10.

Table 6: Average grain size in microns

B10:	38	B5:	34
M10:	44	M5:	32
T10:	45	T5:	41

Phases and misorientation angles remained consistent for all six samples: exhibiting full austenite phase with an average misorientation angle of 34°, indicating uniform crystallographic orientation. In addition, average grain sizes range from 32-45 μm. To further investigate the microstructure, the test piece M10, underwent additional higher magnification EBSD to check for presence of possible δ-ferrite in the boundaries, as shown in Figure 25 a) and b). In this analysis, ferrite was almost non-existent.

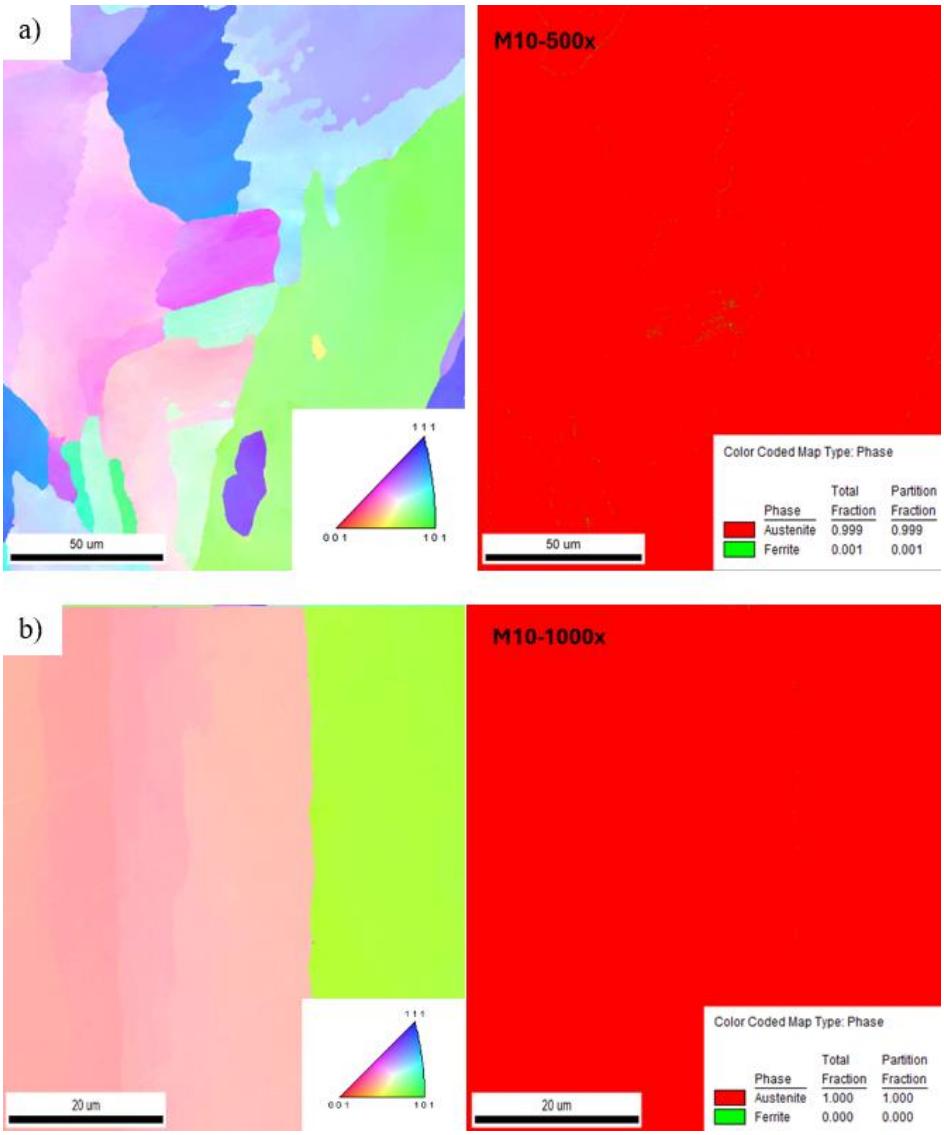

Figure 24: EBSD results of phase content

5.2 Energy Dispersive Spectroscopy Results

5.2.1 Overall Elemental Composition

EDS analysis was carried out on test piece (M10). The findings are summarized in Table 7. In comparison to the original composition from the powder material by MetcoClad (Table 1). There were slight deviations in content of chromium and nickel compared to the powder, a significant reduction was observed in the silicon which decreased by approximately 4.7 times.

Table 7: Chemical composition of material

Element	Al	Si	S	Cr	Mn	Fe	Ni	Mo	Total
Wt %	0.07	0.49	0.01	18.26	1.19	63.63	13.57	2.79	100.0

5.2.2 Oxide Composition

Examination revealed the presence of “holes” of varying sizes, frequently observed at the nanoscale. EDS was utilized to determine these defects and concluded that these holes are composed of manganese-silicon oxides, dispersed randomly throughout the material.

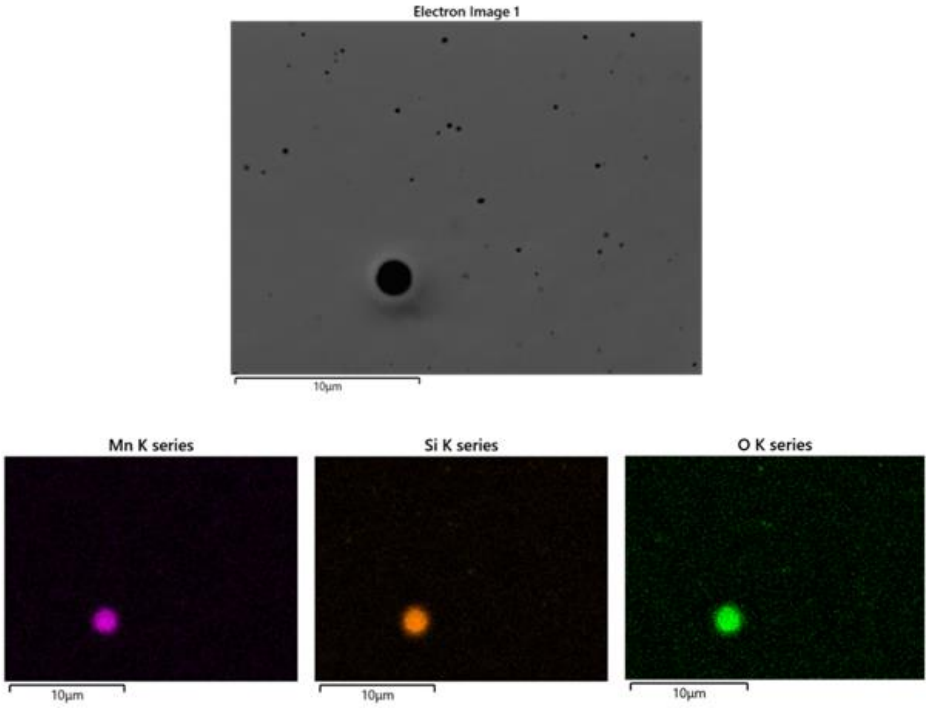

Figure 25: Oxide analysis

5.2.3 Micro segregation Analysis

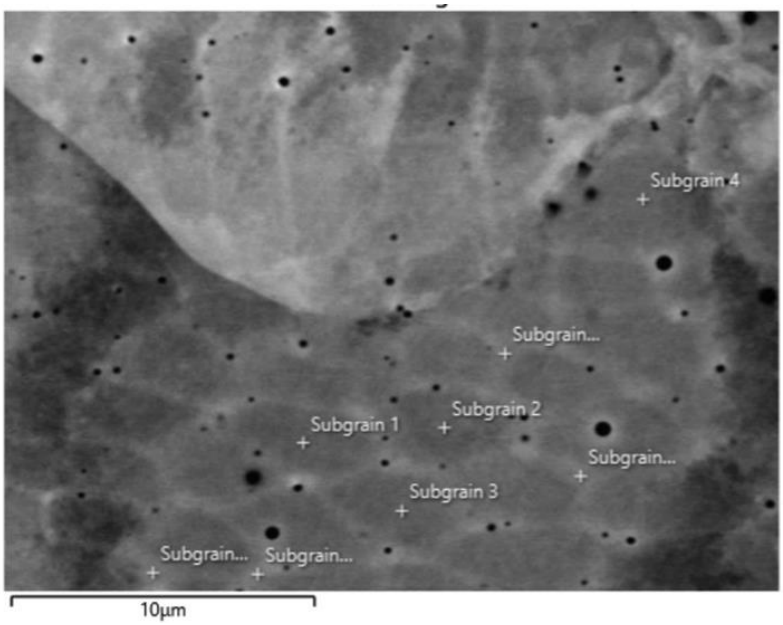

Figure 26: Micro segregation between sub grains and their boundaries

Table 7: Weight percent at each point.

Element in wt%	B. Point 1	B. Point 2	B. Point 3	B. Point 4	C. Point 1	C. Point 2	C. Point 3	C. Point 4	Ratio: B/C
Si	0.53	0.62	0.58	0.61	0.42	0.41	0.47	0.49	1.31
Cr	18.48	18.95	18.93	18.82	17.66	17.67	17.63	17.63	1.07
Mn	1.17	1.23	1.31	1.26	1.02	1.02	1.01	1.04	1.21
Ni	13.55	13.65	13.75	13.68	13.18	13.29	13.25	13.26	1.03
Mo	3.24	3.73	3.54	3.51	2.5	2.35	2.31	2.44	1.46

Micro segregation analysis was conducted with EDS by adding points within the microstructure. Labeled as Boundary Point (B. Point) and Cell Point (C. Point). The values showcased elements such as Si, Mn and Mo exhibited higher ratio (greater wt.% in the boundaries), which indicated a clear accumulation.

5.3 Defects

Figure 27: This figure shows partially melted powder particles, indicating incomplete fusion during the deposition process. This is likely caused by suboptimal laser power or scanning speed, which resulted in the powder material not fully melting and led to defects.

Figure 28a)-b): These figures demonstrate the presence of bonding defects across multiple areas of the material, especially where inner and outer layer (clad layer) intersect. Such interlayer defects contribute to material's porosity and reduce overall density of the material.

Figure 28c): The absence of δ-ferrite in the material, shown from EBSD phase diagrams, suggests that cracks are likely to form. This study is evident here.

Figure 28d): Pores were dispersed throughout the material ranging in different sizes; With length ranging from 90-114 μm in length and 40-65 μm in width. Their presence can reduce overall density.

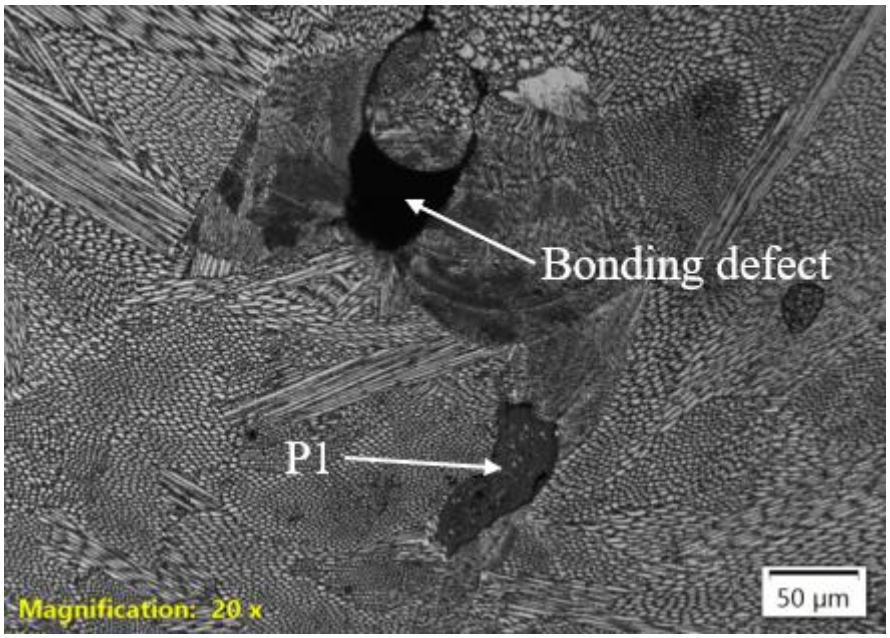

Figure 27: Bonding defect and at P1 the powder is not melted properly

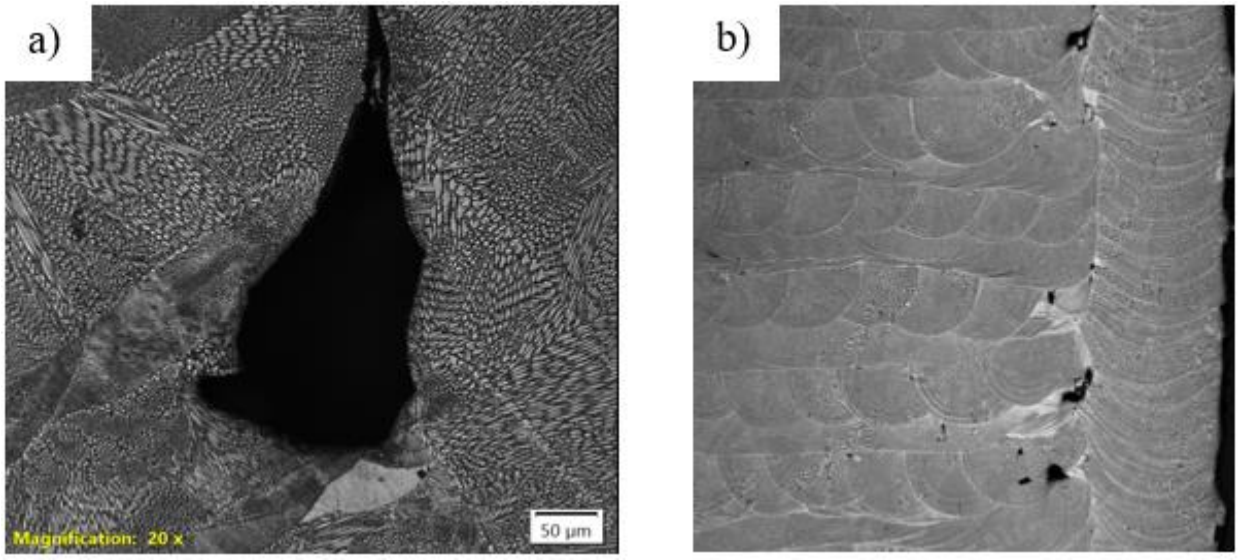

Figure 28: a) Bonding effects and b) meander scan at 2.5x at the transition to outer layer, c) crack and d) pores detected

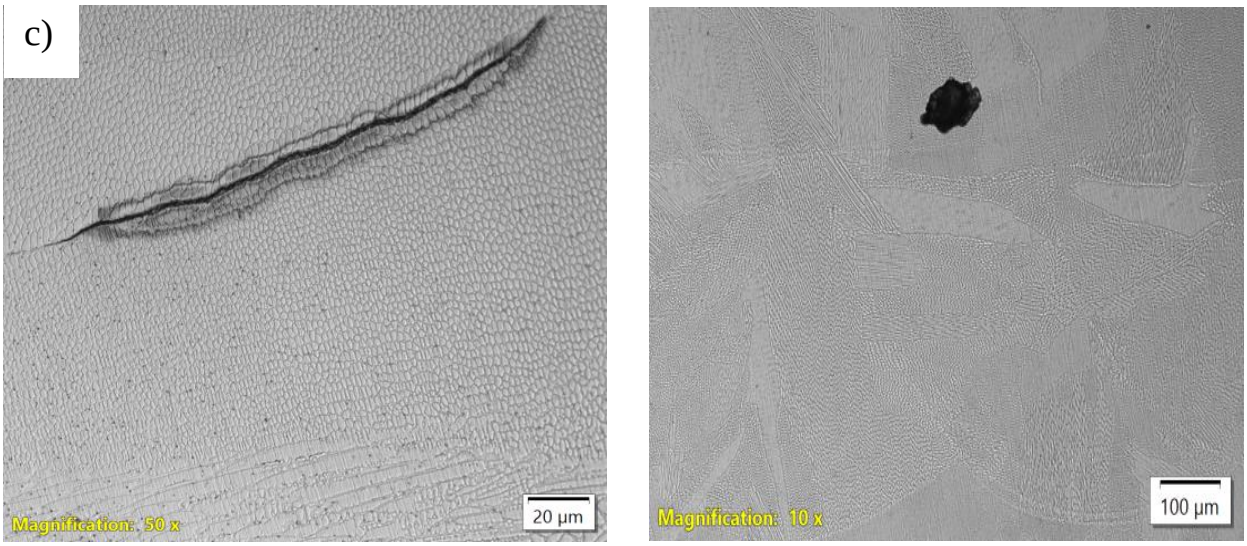

5.4 Impact testing

Table 8: Impact testing results. L1, L2 and L3 perpendicular to build direction. H1, H2 and H3 parallel to build direction.

Test ID	Manual (Joule)	Digital (Joule)
L1	112	111.4
L2	116	115.8
L3	116	115.7
Mean $\pm$ SD	114.7 $\pm$ 2.3	114.3 $\pm$ 2.5
H1	118	118.6
H2	106	104.7
H3	116	114.8
Mean $\pm$ SD	113.3 $\pm$ 6.4	112.7 $\pm$ 7.2

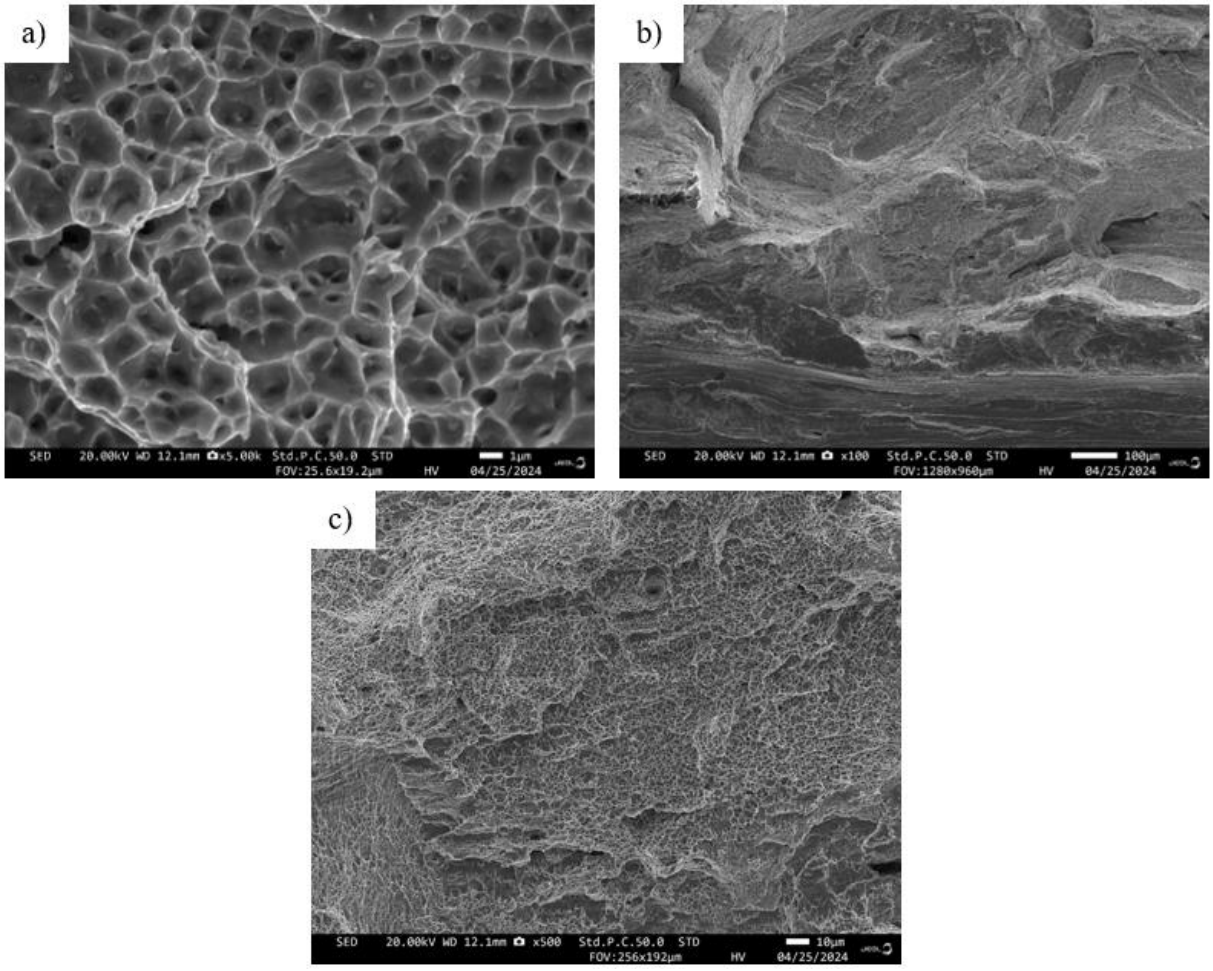

Figure 29: Fracture surface of L1 in SEM, with dimples indicating a ductile fracture

5.5 Hardness Results

Table 9: Hardness results

Region (Total 44 indentation)	Mean ± SD (HV)
Bottom (nr. 1-14 indentation)	203 ± 9.5
Middle (nr. 15-30 indentation)	198 ± 7.5
Top (nr. 31-44 indentation)	200 ± 7.4

The mean Vickers hardness values across all indentations is 200 HV, with the highest recorded at 218 HV and the lowest at 183 HV. There was a standard deviation of 8 HV.

5.6 Porosity Results

Table 10: Porosity results

Test ID	Relative Density (%)
Porosity piece	99.6
L1	99.8
L3	99.8

6 Discussion

6.1 Influence of Cooling Rate

Cooling rates had a major impact on how solidification would occur in the microstructure of 316L LMD. Based on results, rapid cooling rate impeded the formation of δ-ferrite and equiaxed grains, thus resulting in homogenous austenitic microstructure. This outcome is consistent with the literature described that faster cooling rates shortened the time for ferrite formation [7,8,27], thereby solidifying as fully austenitic phase. This phenomenon was observed in the EBSD analysis, showing only a ferrite content of .1%. Guofang Liang et al. studied that faster cooling rates tend to produce finer grains [30]. Finer and smaller grains usually correlate to higher yield strength due to the grain boundary strengthening, Hall-Petch relationship. From the EBSD data, average grain sizes were between 32-45 μm, it is comparable and slightly better than grain-size requirements with forged 316L of around 45-90 μm [31,32]. Furthermore, cooling rate of 6800-8200K/s seemed plausible as J.W. Elmer et al. suggested that laser beam has a range of solidification between 10^2 K/s and 10^6 K/s [8].

6.2 Microstructure

Despite anticipated AF solidification of approx. 10% ferrite via Schaeffler Diagram (Figure 3), the ferrite content was roughly .1% of all six samples mounted for EBSD. This may likely be due to the fast-cooling rate which inhibited δ-ferrite transformation, thus resulting in a homogenous austenitic solidification. The microstructure consists of coarse columnar grains and cellular sub grains in a hexagonal mesh. These columnar grains extend through the fusion boundary causing an epitaxial and directional solidification, which can be seen evidently in Figure 17 and 21. This is because of thermal cycle in which the substrate acts as a heat sink from the molten pool causing grains from the substrate to elongate to the heat flow. In addition, equiaxed grains were barely visible in EBSD. Localized heat affected zones were unnoticeable because of low heat input and high cooling rate in the welded zone [4].

Thermal cycle is apparent within the track-widths and cooling rate of material from 760 μm to 830 μm, 8200K/s to 6800K/s from Bottom to Top region, respectively. On the other hand, since the material exhibits directional solidification causing columnar grains, the grains have a preferential growth orientation. From the pole figure (Figure 23), it is noticeable that it has a texture with a preferred orientation along the <001> direction. However, it is peculiar that the

points are not gathered in the center of <001> suggest that some deviation or tilt in the material from the ideal direction. It may be cause to poor alignment in SEM.

Furthermore, defects were found vastly throughout the material. With varying degrees of pore sizes present but a noticeable and underlying problem was these bonding defects that were apparent in the outer layer (clad layer) adjacent to inner layer. This is likely due to partially melted powder from suboptimal process parameter for these scenarios. Cracks during deposition were found; this is because lack of ferrite making it less resistance to hot cracking. Overall, these defects only account for the process parameters because density analysis revealed that material had a relative density exceeding 99.5%. However, these minor discrepancies were noted, since test piece was larger in dimension in comparison to L1 and L3 combined. And pores and inclusions (oxides) are present. These Mn-Si oxides were dispersed throughout the material in nanometer scale. It is peculiar since the chamber is enclosed with no interference and protected with argon gas, given that NAM utilizes TruLaser Cell 3000 model. It could imply that it may be air entrapped in the powder material during melting.

6.3 Mechanical Properties

The Charpy tests revealed a ductile fracture with dimples, a valid material deformation. Impact values are consistent across x-z and y-z plane notch orientations. However, an anomaly was observed with the SINTEF report [Appendix 3 and 6], where v-notches in the x-y plane had a lower joule value. This discrepancy may be attributed to the material's natural anisotropic behavior. In comparison with the results conducted by SINTEF and us, there is a change in value because ours were performed based on ASTM A182 at a temperature of -18°C [38], thereby concluding that results were in line with expected values.

The anisotropy from tensile tests in the SINTEF report. Yield strength (RP 0.2) for test ID's 10, 11, and 12 were strained parallel to the build direction; showcased a lower yield strength with an average of 257 MPa, lower than to the build direction test pieces that were around 430-500 MPa [Appendix 4]. Mukherjee concluded that anisotropy is attributed to the orientation of columnar grains. If loading direction is parallel to the build direction, dislocation cross fewer boundaries thus resulting in a lower yield strength in z-direction.

Hardness values remained consistent with mean value of 200HV, it could imply that grain sizes in the material remained consistent in the 30-40 microns range with slight deviation because of thermal gradient.

Table 11: Comparison with forged values 316L

	Yield Strength (MPa)	Tensile Strength (MPa)
Z-direction (LMD) [Appendix 4]	418.1 ± 100.8	616.5 ± 17.6
X and Y-direction (LMD) [Appendix 4]	524.2 ± 7.5	663.5 ± 5.4
Y.li et al. (as forged) [44]	305.3 ± 2.6	601.4 ± 5.3
ASM (as forged) [45]	290	560

LMD processed 316L showcase better mechanical properties than as forged. A possible answer is because the additive manufacturing process has controlled grain growth and smaller grain sizes. Anisotropy and epitaxial solidification have always been an issue, as it offers lower yield strength and a standard deviation of 100.8 in z-direction. And instead of having more boundaries, the remelting process of previous substrate caused these columnar grains to expand further making them coarser, thus lower in mechanical properties. Nordic Additive Manufacturing has seen these underlying issues as they offer a lower heat input.

6.4 Further Work

For future work it would be interesting to perform an analysis of corrosion resistance of 316L LMD and compare it to other additive methods and forged 316L. Furthermore, the possible effectiveness of heat treatment for ferrite formation to reduce hot cracking and anisotropy.

7 Summary and Conclusion

The study revealed that cooling rates played a significant role on solidification structure, as faster cooling rates offers reduced presence of ferrite. Because rapid cooling not only inhibited ferrite formation, but it also developed finer grains as well, which is consistent with Hall-Petch relationship. EBSD data further enhanced our understanding, showing reduced grain size. LMD offered slight superiority in mechanical properties over forged ones. However, a big difference in values of where loading direction is located indicated anisotropy, valid from findings in EBSD as well as LOM. These findings can be a steppingstone on further optimizing the process parameters to enhance its structural integrity.

It is confirmed that the 316L produced by NAM exhibit a high-quality austenitic microstructure with excellent density and slightly greater mechanical properties in comparison to conventional forged 316L, although some degree defects were found e.g. pores, cracks, and weak interlayer bonding. These findings do not outweigh the potential of Laser Metal Deposition with material properties comparable to those forged equivalents.

References

[1] W. D. Callister and D. G. Rethwisch, Materials Science and Engineering - Eight Edition, John Wiley & Sons, 2011.

[2] N. Loth, "Directed Energy Deposition (DED) Metal 3d Printing - The Ultimate Guide," *All3DP,* 27 April 2023.

[3] M. Mukherjee, "Effect of build geometry and orientation on microstructure and properties of additively manufactured 316L stainless steel by laser metal deposition," *ScienceDirect,* 2019.

[4] "NAM - Laser Sveising," Nordic Additive Manufacturing, [Online]. Available: https://www.nordicadditive.no/laser-sveising. [Accessed 22 Januar 2024].

[5] Y. Pardhi, "Laser metal deposition - developing new materials," *Sulzer,* p. 2, 2022.

[6] W. F. Hosford, Iron and Steel, Cambridge University Press, 2012.

[7] J. C. Lippold and D. J. Kotecki, Welding Metallurgy and Weldability of Stainless Steel, John Wiley & Sons, 2005.

[8] J. W. Elmer, S. M. Allen and T. W. Eagar, "Microstructural development during Solidification of Stainless Steel Alloys," *Metallurgical Transactions A, journal Article vol. 20,* pp. 2117-2131, October 1989.

[9] E. Vandersluis and C. Ravindran, "Comparison of Measurement Methods for Secondary Dendrite Arm Spacing," *Springer,* 4 January 2017.

[10] Oerlikon - Metco, "Material Product Data Sheet, Austenitic Stainless Steel Powder for Laser Cladding," 2014.

[11] Specialty Steel Industry of North America, "Alloying Elements," [Online]. Available: https://www.ssina.com/education/product-resources/alloying-elements/. [Accessed 22 January 2024].

[12] outokumpo, "The effects of alloying elements," [Online]. Available: https://www.outokumpu.com/en/expertise/stainless-basics/the-effects-of-alloying-elements. [Accessed 24 Januar 2024].

[13] B. Rothstein, "Why is stainless steel not magnetic?," Mead Metals, Inc., 24 October 2019. [Online]. Available: https://www.meadmetals.com/blog/why-is-stainless-steel-not-magnetic. [Accessed 26 Januar 2024].

[14] D. R. Askeland and W. J. Wright, The Science and Engineering of Materials - 7th edition, Cengage, 2019.

[15] Aerospace Specification Metals inc., "AISI Typer 316L Stainless Steel, annealed bar," [Online]. Available:

https://asm.matweb.com/search/SpecificMaterial.asp?bassnum=mq316q. [Accessed 5 February 2024].

[16] thyssenkrupp - materials, "Stainless Steel 316L 1.4404," [Online]. Available: https://www.thyssenkrupp-materials.co.uk/stainless-steel-316l-14404.html. [Accessed 5 February 2024].

[17] EARTHDATA - NASA, "Air Mass/Density," [Online]. Available: https://www.earthdata.nasa.gov/topics/atmosphere/atmospheric-pressure/air-mass-density. [Accessed 5 February 2024].

[18] N. Brubaker, H. Ali, S. Dhakal, N. Van Rooyen, M. Jaster, I. Charit, B. Jaques and M. Maughan, "Investigating Microstructure and Properties of 316L Stainless Steel Produced by Wire-Fe Laser Metal Deposition," *ASM International*, 9 January 2022.

[19] Z. Tan, J. Pang, J. Kaminski and H. Pepin, "Characterization of porosity, density, and microstructure of directed energy deposited stainless steel AISI 316L," *Elsevier* , pp. 286-296, 16 November 2018.

[20] H. Hu, "Texture of Metals," *Gordon and Breach Science Publishers Ltd.*, pp. 233-258, 1 March 1974.

[21] P. Guiraldenq and O. Duparc, "The genesis of the Schaeffler diagram in the history of stainless steel," *Metallurgical Research Technology*, pp. 1-9, 18 July 2017.

[22] J. Malczyk, "Gas (Helium) Pycnometer Theory and Practice," *InstruQuest, Inc.*, January 2019.

[23] Oxford Instruments, "What is Electron Backscatter Diffraction (EBSD)?," [Online]. Available: https://www.ebsd.com/ebsd-explained/what-is-ebsd. [Accessed 4 March 2024].

[24] A. Nanakoudis, "EDX Analysis with SEM: How Does it Work?," ThermoFisher, 28 November 2019. [Online]. Available: https://www.thermofisher.com/blog/materials/edx-analysis-with-sem-how-does-it-work/. [Accessed 4 March 2024].

[25] A. Nanakoudis, "SEM: Types of Electrons and the Information They Provide," ThermoFisher, 21 November 2019. [Online]. Available: https://www.thermofisher.com/blog/materials/sem-signal-types-electrons-and-the-information-they-provide/. [Accessed 4 March 2024].

[26] University of Cambridge, "Dendritic Growth," [Online]. Available: https://www.doitpoms.ac.uk/tlplib/solidification_alloys/dendritic.php. [Accessed 10 March 2024].

[27] J. W. Fu, Y. S. Yang, J. J. Guo and W. H. Tong, "Effect of cooling rate on solidification microstructures in AISI 304 stainless steel," *Material Science and Technology*, pp. 265-273, August 2008.

[28] A. Basak and S. Das, "Epitaxy and Microstructure Evolution in Metal Additive Manufacturing," *Annual Review of Materials Research*, pp. 125-149, 9 March 2016.

[29] R. H. H.K.D.H. Bhadeshia, Steels: Microstructure and properties, 2017: Butterworth-Heinemann.

[30] G. Liang, Y. Ali, G. You and M.-X. Zhang, "Effect of cooling rate on grain refinement of cast aluminium alloys," *ScienceDirect ,* pp. 113-121, 2018.

[31] H. J. Henning, "Grain-Size Requirements with 316L Forgings," NED, 19 June 2008. [Online]. Available: https://www.newequipment.com/metal-forming/article/21923684/grain-size-requirements-with-316l-forgings. [Accessed 2 April 2024].

[32] C. Mukherjee, "Grain size control for successfully fabricating stainless and INCONEL alloy tubing," The Tube and Pipe Journal, 21 November 2016. [Online]. Available: https://www.thefabricator.com/tubepipejournal/article/tubepipeproduction/grain-size-control-for-successfully-fabricating-stainless-and-inconel-alloy-tubing. [Accessed 2 April 2024].

[33] "Additive Manufacturing Research Group," Loughborough University, [Online]. Available: https://www.lboro.ac.uk/research/amrg/about/the7categoriesofadditivemanufacturing/. [Accessed 15 April 2024].

[34] H. Hartvigsen, R. Larentsen, K. Michelsen, S. Seljevoll and E. Neergaard, Verkstedhåndboka, Gyldendal undervisning, 2006.

[35] L. Bjerregaard, K. Geels, B. Ottesen and M. Ottesen, Metalog Guide, Struers A/S, 2002.

[36] M. Aga, *Specification of resulting microstructure from additive manufacturing by Direct Laser Deposition of SS316L-SI on stainless steel base materials,* Stavanger: University of Stavanger, 2018.

[37] *Metallic materials — Charpy pendulum impact test — Part 1: Test method, ISO 148-1:2016,* 2016.

[38] *Standard Specification for Forged or Rolled Alloy and Stainless Steel Pipe Flanges, Forged Fittings, and Valves and Parts for High-Temperature Service, ASTM A182/A182M:23,* 2023.

[39] W. D. Callister, Jr and D. G. Rethwisch, Callister's Materials Science and Engineering, SD Books, 2020.

[40] "Structure of metals and alloys," Pocket Dentistry, 1 January 2015. [Online]. Available: https://pocketdentistry.com/1-4-structure-of-metals-and-alloys/. [Accessed 2 May 2024].

[41] A. Samy, "Solidification of metals," Materiallugy, 31 October 2023. [Online]. Available: https://www.materiallugy.com/2023/10/solidification-of-metals.html. [Accessed 2 May 2024].

[42] D. Kopeliovich, "Solidification," SubsTech, 13 December 2023. [Online]. Available: https://www.substech.com/dokuwiki/doku.php?id=solidification. [Accessed 2 May 2024].

[43] *Metallic materials - Vickers hardness test - Part 1: Test method (ISO 6507-1:2023)*, 2023.

[44] Y. Li, C. Ma, F. Qin, H. Chen, X. Zhao, R. Liu and S. Gao, "The microstructure and mechanical properties of 316L austenitic stainless steel prepared by forge and laser melting deposition," *Elsevier*, pp. 1- 14, 22 February 2023.

[45] "AISI Type 316L Stainless Steel, annealed bar," ASM, [Online]. Available: https://asm.matweb.com/search/SpecificMaterial.asp?bassnum=MQ316N. [Accessed 4 May 2024].

Appendix A – Drawing

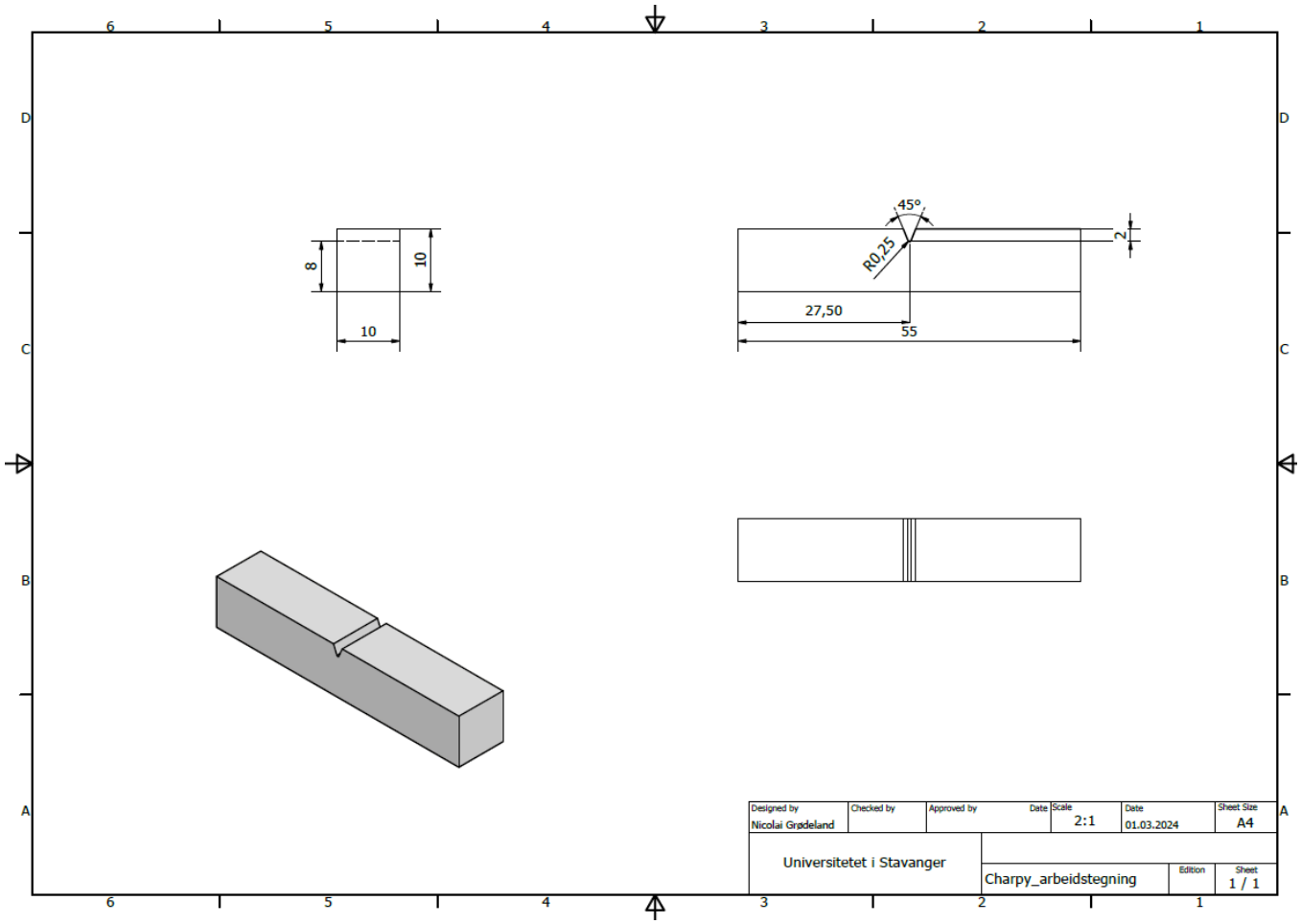

Appendix 1: Working drawing Charpy

Appendix B – Material product data sheet

Quick Facts	
Classification	Alloy, iron-based
Chemistry	Fe 12Ni 17Cr 2.3Mo 2.3Si 1Mn 0.03C
Manufacture	Gas atomized
Morphology	Spheroidal
Service Temperature	≤ 900 °C (1650 °F)
Apparent Density	4.0 – 4.5 g/cm^3
Purpose	Corrosion protection, creep and stress-rupture resistance at elevated temperatures
Process	Laser Cladding

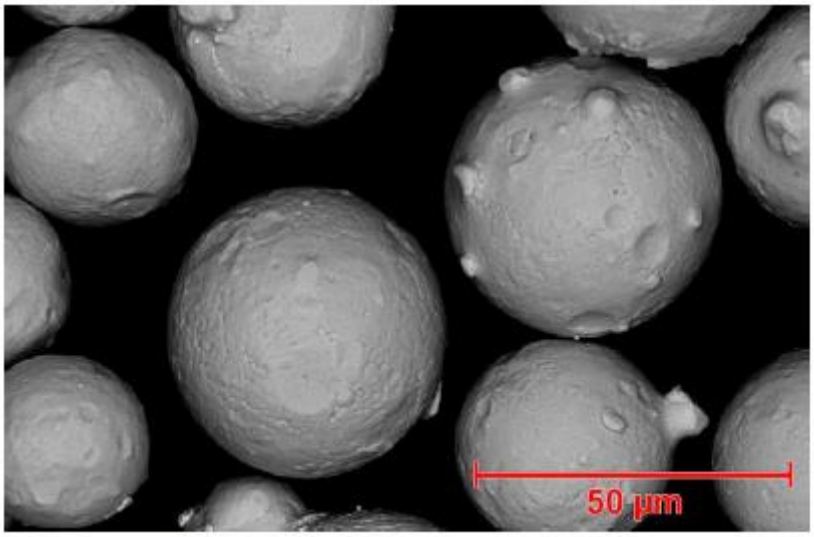

Typical Morphology of MetcoClad 316L-SI Powder

Appendix 2: Summary of austenitic stainless-steel powder

Appendix C – SINTEF

Prøve ID	Avlest energiopptak [kpm]	Multiplikasjonsfaktor	Slagseighet KV/KU [J]
7	13,4	9,81	131
13	13,8	9,81	135
14	14,3	9,81	140
15	14,8	9,81	145
16	14,0	9,81	137
17	13,2	9,81	129
18	13,4	9,81	131
19	12,0	9,81	118
20	11,0	9,81	108
21	12,1	9,81	119
22	14,8	9,81	145
23	14,8	9,81	145
24	14,9	9,81	146
25	14,8	9,81	145
26	14,8	9,81	145
27	14,8	9,81	145
39	10,7	9,81	105
40	12,7	9,81	125
41	7,5	9,81	74
42	13,3	9,81	130
44	12,7	9,81	125

Appendix 3: Charpy table, test done at 20ºC according to ISO 148-1:2016

	identification	S0	L0	Rp 0,2	Rm	Ag	A	HRC	(Z) %
Nr		mm²	mm	MPa	MPa	%	%		
1	1	12,51	19,96	502	635	24,3	37,2	48	68
2	2*	12,39	19,86	517	638	21,8	35,9	48	68
3	3*	12,51	19,96	502	640	21,9	32,1	48	62
4	4	12,56	20,00	515	653	19,1	37,0	48	59
5	5	12,41	19,88	529	666	20,1	40,4	48	63
6	6	12,51	19,96	530	665	18,6	37,4	48	55
7	7	12,57	20,01	528	667	18,7	35,2	48	63
8	8	12,53	19,98	529	667	19,3	34,0	48	59
9	9	12,57	20,01	514	663	19,1	35,6	48	62
10	10	12,48	19,93	249	589	28,3	41,8	48	81
11	11	12,47	19,93	250	589	29,8	43,9	48	82
12	12	12,28	19,77	273	596	27,2	40,5	48	83
13	33	12,55	19,99	433	610	25,7	42,3	48	59
14	34	12,55	19,99	437	617	24,8	40,7	48	59
15	35	12,50	19,95	434	618	25,6	43,6	48	71
16	36	12,61	20,04	473	622	18,5	36,7	48	67
17	37	12,37	19,84	472	622	18,9	36,0	48	66
18	38	12,46	19,92	475	622	19,2	36,2	48	67

Appendix 4: Tensile testing table, tensile test according to ASTM-E8/E8M-22

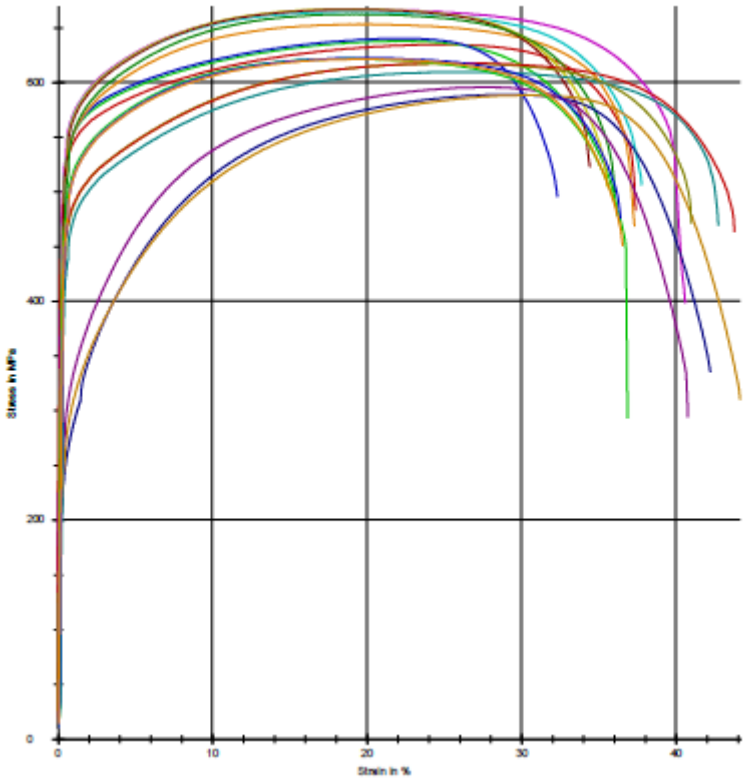

Appendix 5: Stress/strain tensile

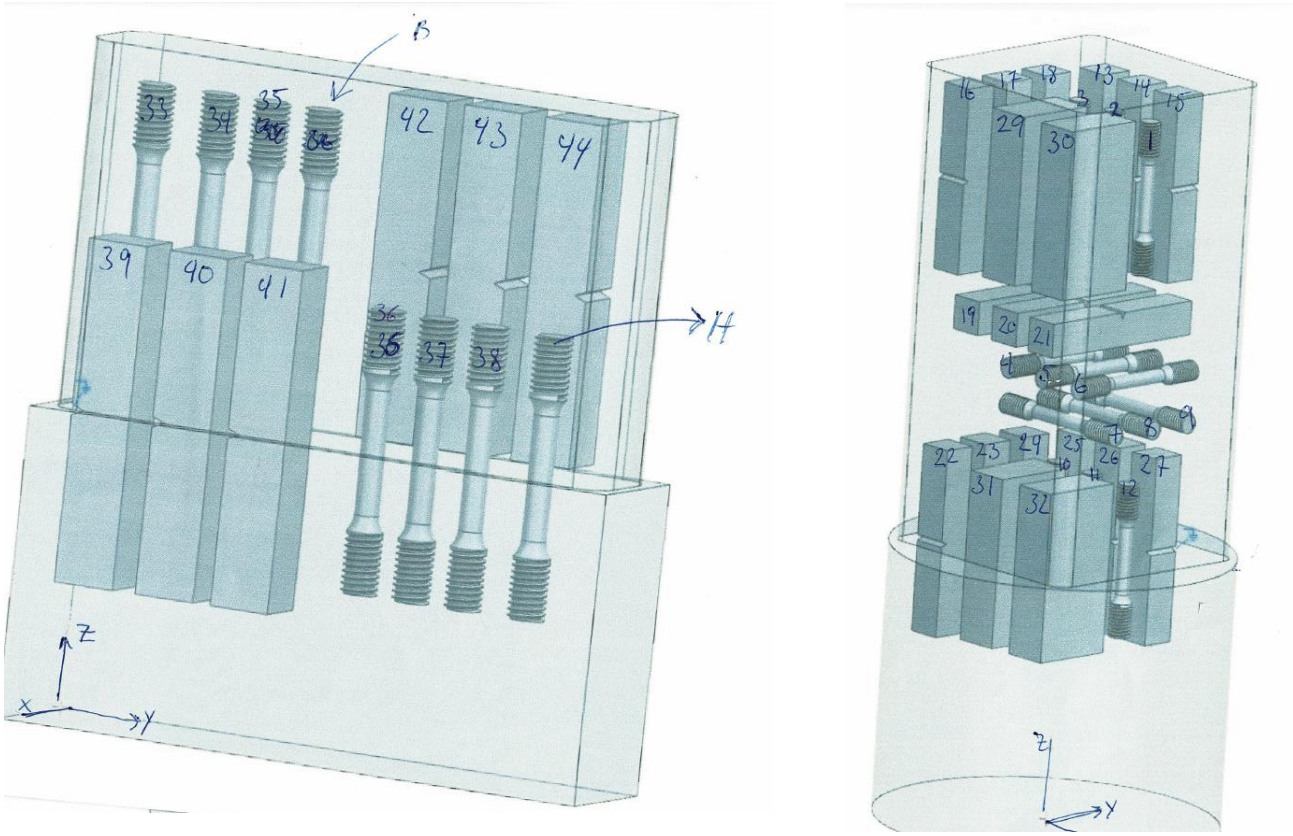

Appendix 6: Orientation of specimens

Test Plan: Thick Test Specimen (ATB)

70x70 LMD on base

Test No.:	Test	Comments	Test No.:	Test	Comments
BPQ0010-1	Tensile		BPQ0010-13	Sharpy	
BPQ0010-2	Tensile		BPQ0010-14	Sharpy	
BPQ0010-3	Tensile	Macro structure assesment on end of part	BPQ0010-15	Sharpy	Macro Structure assesment on end of part
BPQ0010-4	Tensile		BPQ0010-16	Sharpy	
BPQ0010-5	Tensile		BPQ0010-17	Sharpy	
BPQ0010-6	Tensile	Hardness test on end of part	BPQ0010-18	Sharpy	Hardness test on end of part
BPQ0010-7	Tensile		BPQ0010-19	Sharpy	
BPQ0010-8	Tensile		BPQ0010-20	Sharpy	
BPQ0010-9	Tensile	Micro structure assesment on end of part	BPQ0010-21	Sharpy	Microstructure assesment on end of part
BPQ0010-10	Tensile		BPQ0010-22	Sharpy	
BPQ0010-11	Tensile		BPQ0010-23	Sharpy	
BPQ0010-12	Tensile		BPQ0010-24	Sharpy	
			BPQ0010-25	Sharpy	
			BPQ0010-26	Sharpy	
			BPQ0010-27	Sharpy	
			BPQ0010-28	Sharpy	
			BPQ0010-29	G48	
			BPQ0010-30	G48	Chemical analysis (PMI) on part
			BPQ0010-31	G48	NDT on part
			BPQ0010-32	G48	NDT on part

Test Plan: Thin Test Specimen (ATB)

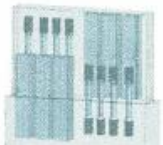

20x96 LMD on base

Test No.:	Test	Comments	Test nummer	Test	Comments
BPQ0010-33	Tensile		BPQ0010-39	Sharpy	
BPQ0010-34	Tensile	Macro structure assesment on end of part	BPQ0010-40	Sharpy	Macro structure assesment on end of part
BPQ0010-35	Tensile	Hardness test on end of part	BPQ0010-41	Sharpy	Hardness test on end of part
BPQ0010-36	Tensile		BPQ0010-42	Sharpy	NDT on part
BPQ0010-37	Tensile	Micro structure assesment on end of part	BPQ0010-43	Sharpy	Micro structure assesment on end of part
BPQ0010-38	Tensile		BPQ0010-44	Sharpy	NDT on part

Appendix 7: Overview

Appendix D – Hardness

Measurement Tables

Pattern: 1

Measurement Index	Result
1 (1/1)	212 HV10
2 (1/1)	212 HV10
3 (1/1)	201 HV10
4 (1/1)	196 HV10
5 (1/1)	194 HV10
6 (1/1)	215 HV10
7 (1/1)	215 HV10
8 (1/1)	208 HV10
9 (1/1)	191 HV10
10 (1/1)	206 HV10
11 (1/1)	202 HV10
12 (1/1)	205 HV10
13 (1/1)	183 HV10
14 (1/1)	208 HV10
15 (1/1)	215 HV10
16 (1/1)	202 HV10
17 (1/1)	188 HV10
18 (1/1)	205 HV10
19 (1/1)	204 HV10
20 (1/1)	191 HV10
21 (1/1)	194 HV10
22 (1/1)	201 HV10
23 (1/1)	197 HV10
24 (1/1)	205 HV10
25 (1/1)	194 HV10
26 (1/1)	193 HV10
27 (1/1)	197 HV10
28 (1/1)	198 HV10
29 (1/1)	186 HV10
30 (1/1)	192 HV10
31 (1/1)	195 HV10
32 (1/1)	196 HV10
33 (1/1)	187 HV10
34 (1/1)	203 HV10
35 (1/1)	205 HV10
36 (1/1)	211 HV10
37 (1/1)	187 HV10
38 (1/1)	199 HV10
39 (1/1)	202 HV10
40 (1/1)	207 HV10
41 (1/1)	194 HV10
42 (1/1)	208 HV10
43 (1/1)	201 HV10
44 (1/1)	204 HV10

Statistics

Pattern	Mean	Min	Max	SD	Range	USL	LSL	Cp	Cpk
1	200	183	215	8	32	0.00	0.00	0	-8

Appendix 8: Data retrieved from InnovaTest Falcon 5000